A Mathematical Model of A Large Open Fire

P.T. Harsha
W.N. Bragg
R.B. Edelman

NASA

A Mathematical Model of A Large Open Fire

P.T. Harsha
W.N. Bragg
R.B. Edelman
Science Applications, Inc.
Canoga Park, CA 91303

NASA

National Aeronautics and
Space Administration

Ames Research Center
Moffett Field, California 94035

CONTENTS

LIST OF FIGURES

iv

1. INTRODUCTION

Because of the high-strength for light-weight capability of carbon
fiber/epoxy structural materials, a significant increase in their use in
commercial aircraft structures has been stimulated by the positive effect on
fuel conservation that the use of such structures would produce. However,
massive utilization of new materials must be preceded by a thorough examination
of any potential hazard created by their use. In the case of carbon fiber
materials, a potential hazard connected with the release of fibers into the
atmosphere in an aircraft accident resulting in fire was identified.

A necessary part of the hazard evaluation (which has been completed
and is reported in Ref. 1) is the determination of the detailed characteristics
of large liquid-fuel pool fires. In a possible post-accident scenario, fibers
are released through consumption of the epoxy matrix in the lower regions of
the fire, and are transported up in the fire plume, until they become entrained
by atmospheric winds. The effective source of fibers from the standpoint of the
atmospheric dispersion process can thus be significantly above ground level,
but the altitude to which a given fiber is carried depends on both the fiber
characteristics and the characteristics of the fire itself. Further, the fibers
can themselves be consumed within the fire, with the amount consumed dependent
on the local temperature and fiber residence time in the interior of the fire
plume.

To provide the detailed prediction of the characteristics of a large
liquid-fuel pool fire that is necessary for adequate determination of the
distribution of fibers that would be entrained by atmospheric winds, a
mathematical model of a liquid fuel pool fire was developed by SAI. The
characteristics of the mathematical model were dictated both by the detail
required to obtain the desired result and by constraints on the time and
resources available to complete the analysis. Since fiber distribution and
consumption were necessary results, a relatively simple, one-dimensional fire
model such as has been reported by Brzustowski (Ref. 2) and by others was not
suitable. On the other hand, the general solution of the liquid-fuel pool
fire problem involves the numerical integration of the three-dimensional
time-dependent, elliptic, Navier-Stokes equations with finite-rate chemical

kinetics, and the general problem is further complicated by the fact that the rate of vaporization of fuel is itself a function of the thermal environment including back-radiation from the fire to the fuel pool.

A tractable mathematical formulation of the pool fire problem can be developed if a number of fundamental assumptions are made. In particular, if it is assumed that the fuel vaporization rate can be independently specified, (and is constant) and that the fire plume is axisymmetric, the problem can be formulated as two-dimensional and steady-state. If it is further assumed that over the bulk of the region of interest gradients in the dependent variables are much larger in the radial direction than in the axial direction, and the static pressure is uniform, the parabolic boundary layer form of the governing equations can be used. This assumption is certainly not valid in the region near the base of the fire, where the ground plane constraint results in entrainment at nearly right angles to the fire plume, but can be expected to be reasonably well-satisfied in the buoyancy-dominated upper plume. The parabolic plume modeled with the analysis described in this report thus represents a simplified analog of a pool fire in a no-wind situation. Although simplified and specialized to the no-wind case, the plume model incorporates considerable detail, including radial and axial velocity, temperature, and species mass fraction profiles, as well as detailed fiber distributions in all parts of the fire flowfield. Initial fiber flow (insertion) rates are based on empirical data for the consumption of the fiber matrix, and are assumed temporally but not necessarily spatially uniform.

Within the overall plume model, submodels are required for the turbulent mixing process, for gas-phase and fiber consumption chemistry, for particulate transport (which includes soot as well as fibers), and for thermal radiation from the fire to its surroundings. Each of these submodels is described in detail in this report. Briefly, the turbulent mixing process is modeled using an eddy viscosity approach; gas-phase chemistry is described with a complete-combustion equilibrium model which assumes different products for regions of the plume which are at different local fuel-air ratios; fiber (and soot) consumption is treated through the use of a one-step global finite-rate chemistry model; and thermal radiation is modeled using a simple optically-thin gas approximation. Particulate transport is modeled by discretizing the

particulate size distribution into a number of classes, each of which is treated as a continuum specie. The particles are assumed to be in thermal equilibrium with the gas phase, and to move in concert with the mean gas phase motion, but can diffuse through the flow at a rate which differs from the gas-phase diffusion rate. Buoyancy effects are included in the formulation of the gas-phase momentum and thermal energy equations, but effects of buoyancy on the turbulent structure of the flow are neglected. These latter effects are in any case not well understood.

Initial results obtained through the use of this model were described in an interim technical progress report, Ref. 3. This work showed that the fire problem is highly nonlinear, so that simultaneous solution of the governing differential equations describing the transport of momentum, energy, and gas phase and particulate species, including the terms representing interphase transport of momentum, energy, and species is necessary to obtain an accurate characterization of the flowfield. Fiber consumption within the fire was shown to occur, and to be especially significant for small fibers. The initial spatial location of the fibers at the point of release was shown to have negligible effects on the distribution of fibers in the plume above the flame zone, within the limits investigated under the axisymmetric assumption.

At the time that the work described in Ref. 3 was completed, no large-scale pool fire data existed with which to compare and validate the fire model. Thus although the results obtained appeared to be qualitatively correct, no quantitative agreement of the results with experimental data could be adduced. This, and the large number of assumptions inherent in the model (some of which were made necessary by the lack of available experimental data) led to the definition, by NASA, of an experimental program to measure the characteristics of large scale pool fires. In this experimental program, radial temperature and species concentration profiles were measured at a number of axial locations within the fire plume, for pool fires of 7.5 and 15 meter diameters (25 and 50 feet), from near ground level to 21 meters (70 feet) above the fire. The instrumentation and their locations were laid out based in part on the results of the initial fire calculations reported in Ref. 3.

The results of the NASA experimental program, carried out at the White Sands (NM) test facility, showed that the initial pool fire computational results were qualitatively correct, but that improvements to the model in several

areas were required to obtain better quantitative agreement. In particular, these results showed that both the turbulent mixing and gas-phase chemistry submodels required improvement. Improvement with respect to the overall mixing rate in the plume was achieved through modifications to the eddy viscosity formulation used: although in general higher-order closures (turbulent kinetic energy models) can be expected to provide better predictions of the overall mixing rate in a turbulent flow than eddy viscosity formulations, the additional complexity of such models is not warranted in the present context because of the number of other assumptions already present in the analysis. The experimental results also showed that the chemical kinetic processes which take place within the fire plume occur in a considerably different manner than is predicted by the local complete combustion equilibrium model used in the analysis. In part this difference is created by finite-rate chemical kinetics effects, but turbulent unmixedness seems also to play a major role. While substantial changes to the chemistry submodel in the fire plume model cannot be made without introducing significant (and again probably unwarranted) complexity, a simple "unmixedness" model was incorporated, substantially improving several aspects of the comparison between the model predictions and the experimental data.

Results of this preliminary work on the improvement of the pool fire model were described in Ref. 4. For certain variables, such as temperature, good agreement between model predictions and the experimental data was demonstrated. However, the overall fuel consumption rate predicted by the model was still far greater than that observed in the experiments, and the temperatures predicted to exist in the highly fuel-rich portion of the fire were substantially higher than those measured. Thus an additional model improvement effort was undertaken, focusing on improvement to the prediction of species distributions within the fire. It was recognized at the outset of this work that complete agreement between the model predictions and the experimental results could not in all likelihood be achieved, within the limits of the complete-combustion equilibrium chemistry formulation assumed. More detailed chemical kinetic models can be postulated, but neither detailed nor global kinetic schemes have yet been demonstrated for the very fuel-rich conditions that pertain in the lower regions of the plume. Even if such chemistry models existed, their incorporation would not be warranted because of the crudity of the treatment of the fluid-mechanical processes inherent in the model in this region.

For these reasons, the model improvement effort focused on the prediction (using an equilibrium formulation) of temperature and species distributions in very fuel-rich regions, and the refinement of the unmixedness formulation described in Ref. 4.

All of the work carried out to develop a usable mathematical model of large-scale open pool fires in a zero-wind environment is summarized in this report, which thus supersedes Refs. 3 and 4. A detailed description of the model is given in Section 2, including the basic equation formulation, the particle tracking methodology, and the gas phase and particulate chemistry submodels, as well as the turbulent mixing and unmixedness submodels, and the radiation submodel. The effects of parameter variation in these submodels are also discussed. This section concludes with a discussion of the limitations of the parabolic formulation of the pool fire problem: while, as noted earlier, much more general formulations of the problem can be defined, these more general formulations are quite complex and some of the inherent complexities are also discussed.

The results of this work are described in Section 3 of this report. These results include predicted profiles of velocity, temperature, and concentrations of O_2 and other species within the plume. Computations of fires for pool sizes ranging from 3.75 to 15 meters (12.5 to 50 feet) are presented, to provide insight into the expected scaling of pool fire phenomena. Where possible, the predicted profiles are compared with experimental data obtained from the NASA/White Sands test program. Section 4 then provides results pertaining to predicted carbon fiber distributions and fiber consumption rates for the fire sizes computed.

Overall conclusions of this modeling program are presented in Section 5. This work has produced a model of pool fire phenomena which, although approximate, is capable of providing considerable detail particularly with respect to expected temperature distributions. While the model has been compared with only a limited amount of experimental data, these data provide the most complete experimental detail on large-scale pool fires that is currently available.

NOMENCLATURE

a_2	coefficient in expression for turbulent kinetic energy dissipation rate, Eq. 44
d_j	diameter of jth particulate specie
e	turbulent kinetic energy per unit mass
$e_{b\lambda}$	monochromatic emissive power, Eq. 46
f	coefficient in unmixedness model, Eq. 45
g	gravitational acceleration
G	particulate species mass fraction vector
h $\left\{\begin{array}{l} \\ \\ \end{array}\right.$	static enthalpy vertical distance above fire pool
H	total enthalpy
J	mechanical equivalent of heat
k	constant in Ferri eddy viscosity model, Eq. 10
k_A	constant in Alpinieri viscosity model, Eq. 12
k_v	initial velocity coefficient, Alpinieri viscosity model, Eq. 12
k_λ	monochromatic volumetric absorption coefficient, Eq. 46
K_p^B	equilibrium constant, Boudouard reaction, Eq. 39
ℓ_k	turbulent viscosity length scale
m_j	mass of jth particulate specie
N	particulate number density vector
P	pressure
P_{O_2}	partial pressure of oxygen
P_{CO}	partial pressure of carbon monoxide
P_{CO_2}	partial pressure of carbon dioxide
Pr	turbulent Prandtl number
q_r	radiative heat flux
$q_{r\lambda}$	radiative heat flux at wavelength λ
r	radial coordinate
r_p	particle radius
r_s	Sauter mean radius
$r_{1/2}$	flowfield half-radius, Eq. 11

R	$\begin{cases} \text{universal gas constant} \\ \text{particulate radius vector} \end{cases}$
Sc	turbulent Schmidt number
T	temperature
u	axial mean velocity
u'	axial velocity fluctuation
v	radial mean velocity
v'	radial velocity fluctuation
W	molecular weight
$\dot{W}_{gi}$	production rate of ith gas-phase specie due to homogeneous gas phase reactions
$\dot{W}_{Pij}^{F}$	production of ith gas phase specie from j^{th} particle class
$\dot{W}_{Pj}^{F}$	production of jth particle class
x	axial coordinate

Subscripts

c	centerline
e	ambient
g	gas-phase
i,j	species indices
p	particulate-phase

Greek Symbols

α	molar atom concentration
β	species mass fraction
$\tilde{\beta}$	element mass fraction
δ	ratio of particle to gas phase eddy diffusivity for energy
ϵ_{Dg}	scalar turbulent gas phase diffusivity
ϵ_{vg}	turbulent eddy viscosity, gas phase
θ	ratio of particle to gas phase species eddy diffusivities
μ_T	turbulent dynamic viscosity
ρ	density
σ	ratio of particle to gas phase eddy viscosity
τ_T	turbulent shear stress

2. TECHNICAL DISCUSSION

The modeling of the physical and chemical processes occuring in a pool fire with the presence of carbon fiber particles involves consideration of a number of basic physical mechanisms. These mechanisms include diffusion, inertia, viscosity, chemistry, chemical kinetics, buoyancy, turbulent transport, and the transport of particulate material. Following the modeling philosophy outlined in the Introduction, we restrict our attention to the axisymmetric (zero-wind) fire problem, with a specified rate of fuel vaporization. With this restriction, the computation becomes one of an axisymmetric, buoyant, two-phase jet flow. The formulation thus becomes that appropriate for the boundary-layer approximation to the equations of motion.

2.1 DESCRIBING EQUATIONS

For an axisymmetric, turbulent, two-phase flow including buoyancy effects and satisfying the boundary layer approximations, the governing equations can be written, following Ref. 5, in the following manner:

Global Continuity

$$\frac{\partial r\rho u}{\partial x} + \frac{\partial r\rho v}{\partial r} = 0 \tag{1}$$

Axial momentum

$$\rho u \frac{\partial u}{\partial x} + \rho v \frac{\partial u}{\partial r} = \frac{1}{r} \frac{\partial}{\partial r} \left\{ r\rho \varepsilon_{vg} \left(\beta_g + \sum_j \sigma_j \beta_{pj} \right) \frac{\partial u}{\partial r} \right\} + g(\rho_e - \rho) \tag{2}$$

in which x and r are the coordinates normal and parallel to the ground plane, respectively (see Fig. 1); u and v are the velocity components in the x- and r-directions, ε_{vg} is the gas phase eddy viscosity (to be described in more detail in Section 2.2), ρ the local density, β_g the mass fraction of all <u>gas-phase</u> species in the multicomponent system, σ_j the ratio of the particulate phase eddy viscosity (diffusion coefficient) for the jth particle-class to the gas phase eddy viscosity, β_j the mass fraction of particulate phase species j, g the gravitational constant, and ρ_e the ambient density;
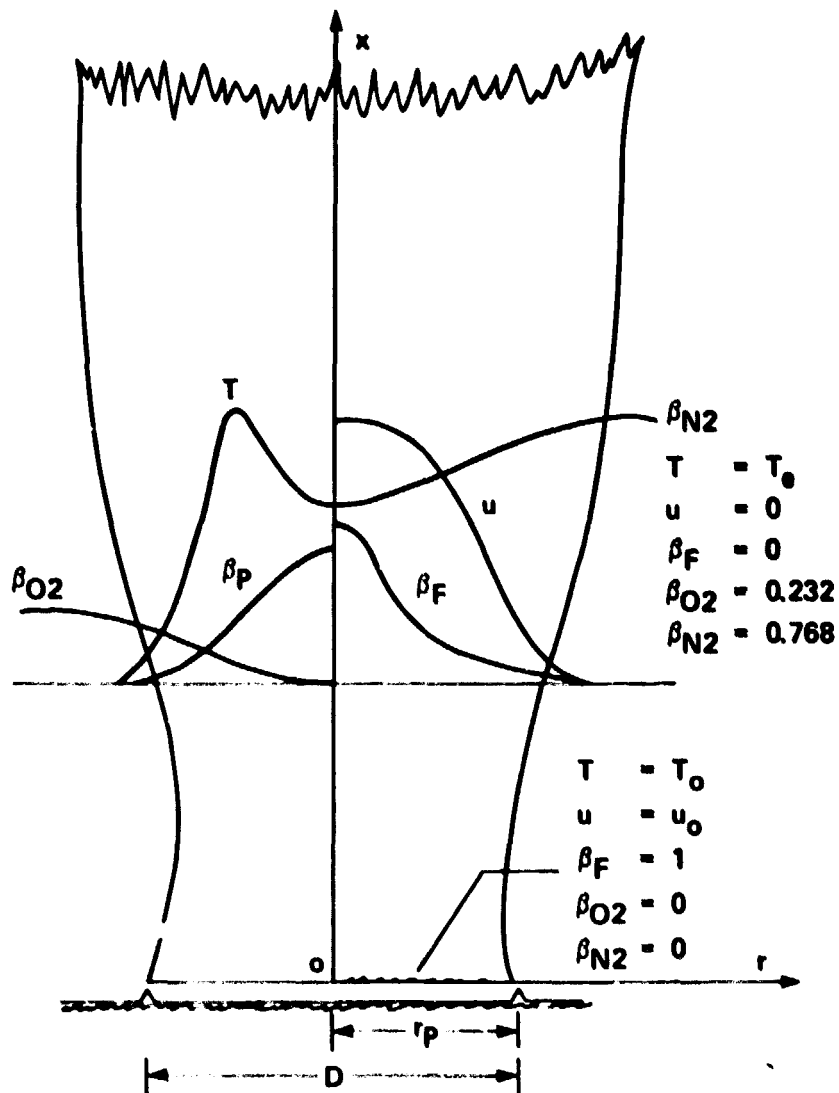
FIGURE 1. Fire Flowfield Schematic and Definition Sketch.

Species Diffusion

i^{th} gas-phase species

$$\rho u \frac{\partial \beta_{gi}}{\partial x} + \rho v \frac{\partial \beta_{gi}}{\partial r} = \frac{1}{r} \frac{\partial}{\partial y} \left\{ r\rho\varepsilon_{Dg} \left[\frac{\partial \beta_{gi}}{\partial r} - \beta_{gi} \left(\frac{(1-\sum_j \theta_j \beta_{pj})}{\beta_g} \frac{\partial \beta_g}{\partial r} + \sum_j \theta_j \frac{\partial \beta_{pj}}{\partial r} \right) \right] \right\}$$

$$+ \overset{\bullet}{W}_{gi} + \sum_j \overset{\bullet}{W}^F_{pij} \tag{3}$$

j^{th} particulate class

$$\rho u \frac{\partial \beta_{pj}}{\partial x} + \rho v \frac{\partial \beta_{pj}}{\partial r} = \frac{1}{r} \frac{\partial}{\partial y} \left\{ r \rho \epsilon_{Dg} \theta_j \left[\frac{\partial \beta_{pj}}{\partial r} - \beta_{pj} \cdot \right. \right.$$

$$\left. \left. \left(\frac{(1 - \sum_k \frac{\theta_k \beta_{pk}}{\theta_j})}{\beta_g} \frac{\partial \beta_g}{\partial r} + \sum_k \frac{\theta_k}{\theta_j} \frac{\partial \beta_{pk}}{\partial r} \right) \right] \right\} + \dot{W}_{pj}^F \tag{4}$$

in which

$\dot{W}_{gi}$ = production of the ith gas-phase specie due to homogeneous gas phase reactions

$\dot{W}_{pij}^F$ = production of the ith gas-phase specie from the jth particle class due to evaporation or heterogeneous reactions,

and

$\dot{W}_{pj}^F$ = production of the jth particle class,

and in which the θ_j represent the ratio of particle-to-gas phase eddy diffusivities of mass and ϵ_{Dg} represents the gas phase eddy diffusivity of mass; and

Mixture Energy Equation

$$\rho u \frac{\partial H}{\partial x} + \rho v \frac{\partial H}{\partial r} = \frac{1}{r} \frac{\partial}{\partial r} \left\{ r \rho \epsilon_{vg} \left[\frac{1}{P_r} \frac{\partial H}{\partial r} + \left(h_g \frac{1}{S_c} \sum_j \theta_j \beta_{pj} - \frac{H_g}{P_r} - \frac{1}{P_r} \left(\frac{P_r}{S_c} - 1 \right) h_g \right. \right. \right.$$

$$- \frac{1}{S_c} \sum_j \theta_j h_{pj} \beta_{pj} \frac{\left(1 - \sum_k \frac{\theta_k}{\theta_j} \beta_{p_k} \right)}{\beta_g} \left. \right) \frac{\partial \beta_g}{\partial r} + \frac{1}{P_r} \sum_j \beta_{pj} (\delta_{pj} - 1) \frac{\partial H_{pj}}{\partial r}$$

$$+ \frac{1}{P_r} \left(\frac{P_r}{S_c} - 1 \right) \sum_i h_{ig} \frac{\partial \beta_{gi}}{\partial r} + \sum_j \left[\theta_j \left(\frac{h_{pj} - h_g \beta_g}{S_c} \right) - \frac{H_{pj}}{P_r} \right] \frac{\partial \beta_{pj}}{\partial r}$$

$$+ \left[\beta_g (1 - \frac{1}{P_r}) - \sum_j \beta_{pj} \frac{\delta_j}{P_r} \right] \frac{\partial (u^2/2)}{\partial r} - \frac{1}{S_c} \left(\sum_k \beta_{pj} h_{pj} \right) \left(\sum_k \theta_k \frac{\partial \beta_{pk}}{\partial r} \right) \left. \right] \right\} \frac{-\partial q_r}{\partial r} \tag{5}$$

Where

$$\theta_j = \frac{\epsilon_{Dj}}{\epsilon_{Dg}} \qquad \delta_j = \frac{\epsilon_{Tj}}{\epsilon_{Tg}} \frac{C_{pg}}{C_{pj}} \qquad \sigma_j = \frac{\epsilon_{vj}}{\epsilon_{vg}}$$

in which H represents the total enthalpy of the mixture, h_g the static enthalpy of the gas-phase mixture, Pr the Prandtl number, S_c the Schmidt number, h_j the static enthalpy of species j, δ_j the ratio of particle-to-gas eddy diffusivity for energy, and q_r represents the radiative heat flux from the flow field.

The mixture energy equation, Eq. (5), may not in general be sufficient to define the thermal state of the system. Only in the case of inert particles (non-radiating) is there similarity in particle drag and heating processes for which "near" dynamic equilibrium would imply "near" thermal equilibrium; if "near" thermal equilibrium does not apply, Eq. (5) must be supplemented by a particulate phase energy equation. However, in the current calculations, the "near" thermal equilibrium assumption has been made. This assumption can be justified by the fact that the bulk of the particulate material present in the fire plume is soot. Because of the very small size of individual soot particles, they rapidly achieve thermal equilibrium with the gas phase even though they are responsible for the bulk of the radiative heat loss from the fire. The larger classes of fibers, which do not rapidly approach thermal equilibrium, constitute only a very small fraction of the flow, in terms of both mass and energy loss. It has also been assumed that the values of θ_j and δ_j appearing in these equations are unity and that $Pr = S_c = 1$.

Eqs. (1) - (5) embody several assumptions in the form in which they are written. These assumptions include:

1. The turbulent shear stress can be represented by an eddy viscosity model.
2. The particulate phase species form a dilute, continuum-like suspension in the multicomponent gas-phase carrier.
3. The volume occupied by the particles is negligible.
4. The particulates are classified in terms of size and composition and each class mixes at a rate determined by its ability to respond to the dynamics of the gas-phase motion.
5. Turbulent transport is important only in the direction normal to the primary flow direction, i.e., radially.

In order to close the system of equations, expressions for the eddy viscosity, ε_g, the species production terms $\dot{W}$, and the radiative heat loss q_r must be specified, along with thermal and caloric equation of state. While the thermal and caloric equations of state are given by the equations

11

$$\rho = \frac{P}{RT\Sigma_i (\beta_i/W_i)} \tag{6}$$

and

$$H_g = \Sigma_i h_i + \frac{u^2}{2gJ} \tag{7}$$

models for the remaining terms must be supplied. These models must be both reasonably accurate and sufficiently simple to allow a tractable computation procedure; in view of the other assumptions inherent in the overall pool fire model, great sophistication in the formulation of these submodels is not warranted. On the other hand, the accuracy of the submodels used must be sufficient to obtain a model that will reliably predict the basic details of the fire structure over a useful range of fire sizes. Because of their importance, each of the submodels will be described in detail in the remainder of this section. In addition to the submodels required for the eddy viscosity, the species production terms, and the radiative heat loss, the particle tracking methodology requires careful development for a situation, such as the carbon fiber/pool fire problem, in which the particles are not inert but are themselves burning. The techniques developed to account for particulate mixing and combustion phenomena will also be described in this section.

2.2 TURBULENT TRANSPORT MODELING

As has already been noted, the formulation used in this study includes a turbulent eddy viscosity model, i.e., the turbulent shear stress, τ_T, is written

$$\tau_T = -\overline{\rho u'v'} = \rho \epsilon_g \frac{\partial u}{\partial r} \tag{8}$$

where ϵ_{vg} is a phenomenological "eddy" viscosity. As originally formulated (Ref. 3), the eddy viscosity was defined by an expression postulated by Ferri, et al., Ref. 6, in which

$$\rho \epsilon_{vg} = kr_{1/2} (\rho_c u_c - \rho_e u_e) \tag{9}$$

In this expression, the subscript e refers to evaluation in the ambient environment and the subscript c to evaluation along the flow field centerline. Since for the zero-wind pool fire problem $u_e = 0$, in this case Eq. (9) reduces to

$$\rho \varepsilon_{vg} = k r_{1/2} \rho_c u_c \tag{10}$$

where $r_{1/2}$ is the "half-radius," defined as the distance from the flowfield centerline to the radius at which

$$\rho u = 1/2 (\rho_c u_c + \rho_e u_e) = 1/2 \rho_c u_c \tag{11}$$

Use of Eq. (10) requires specification of the coefficient k: it is characteristic of models of the form of Eqs. (9) and (10) (and other models which relate the eddy viscosity to mean flow field quantities) that the coefficient k is itself a function of the flow field. However, investigation of the prediction of a number of (nonreacting) variable density flowfields using this approach showed that reasonably good results can be obtained for a value of $k \simeq 0.025$ (Ref. 7).

The flow fields utilized in Ref. 7 to investigate the predictive capability of the model given by Eq. (10) were neither reacting nor buoyant. Thus it is not particularly surprising that while, when compared to the data obtained for a 15 meter (50 foot) diameter pool fire in the NASA/White Sands experimental program, the pool fire calculation incorporating Eq. (10) provided predictions in qualitative agreement with the data, quantitative agreement was not achieved. This result is shown on Fig. 2, from which it can be seen that the model underpredicts the rate of mixing in the early part of the tire development and overpredicts the subsequent mixing rate. (The comparison shown in Fig. 2 is with centerline temperature, as are most of the comparative results displayed in this section. Comparisons of model predictions with other data will be described in Section 3 of this report.)

As has already been noted, the coefficient k appearing within the eddy viscosity model defined by Eq. (10) is in general a function of the flowfield; moreover, the use of a "two stage" viscosity model in which the value of k is different in different parts of the flow is a hoary tradition in the application of eddy viscosity models to jets. However, physical constraints limit the
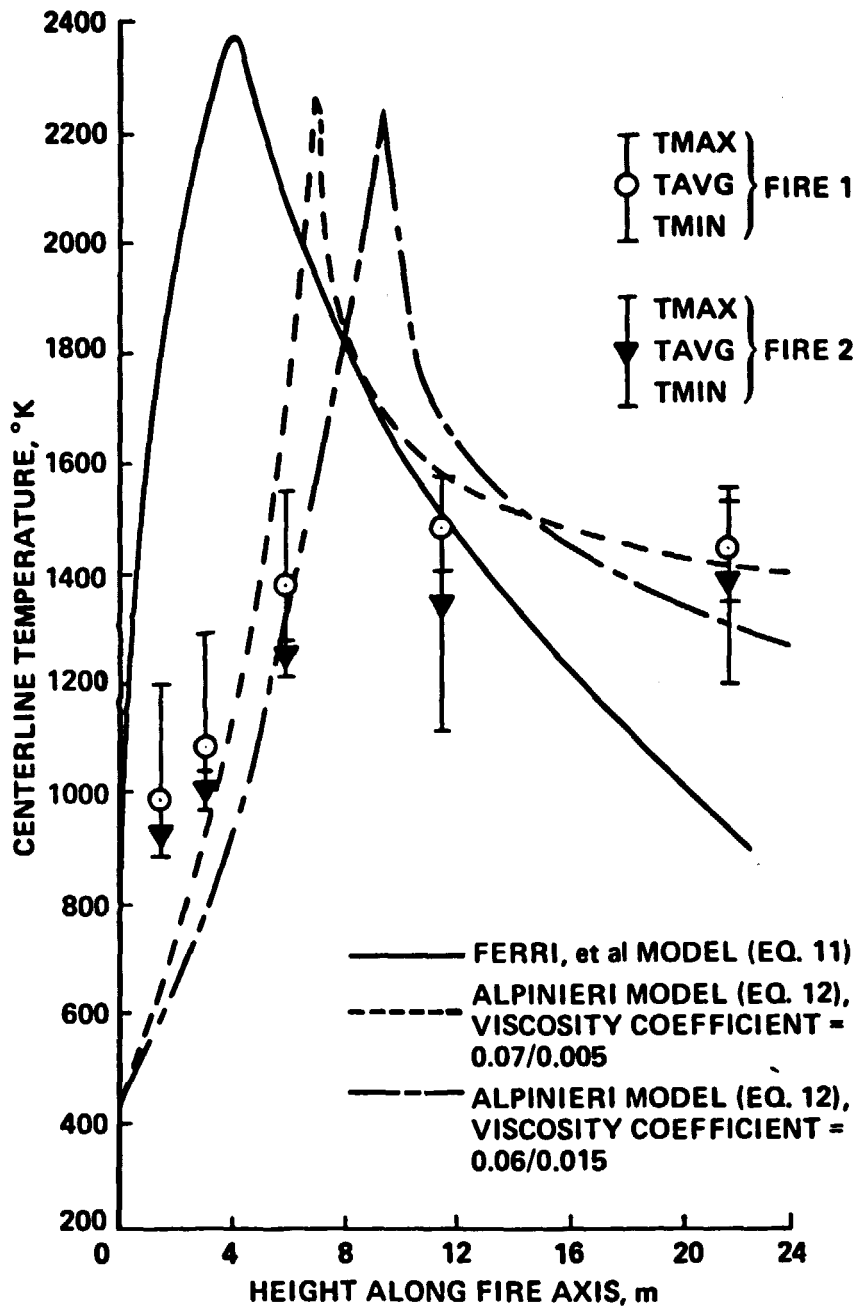
FIGURE 2. Effect of Variation of Eddy Viscosity Model and Eddy Viscosity
Coefficients on Centerline Temperature Prediction,
15 M (50 Foot) Fire.

range of variation in the constant k: for k ≈ 1, the local turbulent shear
stress level approaches parity with the flow field dynamic head, which is a
patently implausible situation. Yet, using Eq. (10), values of k approaching
unity are required to increase the initial mixing rate (given the parabolic
formulation of the problem) to the levels apparent from the experimental results.

From visual and photographic observations of the behavior of large pool
fires it is apparent that these flowfields involve large regions of complex
recirculating flow near ground level. The visual and photographic observations
are supported by measurements which show substantial oxygen concentrations
near the centerline of the fire at heights just above ground level. This
phenomenon can clearly not be rigorously modeled under a parabolic (boundary
layer) approximation. However, an eddy viscosity formulation has been developed
which provides quantitatively correct mixing rate predictions under just such
a situation.

The results of a series of experiments on the mixing of coflowing hydrogen
(inner) and air (outer) streams have been described by Alpinieri (Ref. 8);
this work also involved the development of an eddy viscosity formulation which,
when used with a parabolic mixing model, provided quantitatively correct mixing
rate predictions for these flow fields. The eddy viscosity model described
by Alpinieri is substantially different in form from any other locally (mean
flow) dependent eddy viscosity formulation. An investigation of the details
of the experiments performed by Alpinieri, described in Ref. 7, showed that
this flow field exceeds by a substantial margin the criteria established for
the existence of large-scale recirculation zones within the inner flow. Thus
the rapid mixing rate observed by Alpinieri (Ref. 8) in the initial region of
the flowfield is a result not of turbulent diffusion but of large-scale
convective mixing. The eddy viscosity model described by Alpinieri is then
not a model for the turbulent diffusivity but (in the initial region of the
flow) a correlation, which in conjunction with a parabolic analysis, provides
a substantially better simulation of a flow with large-scale near-field
recirculation regions.

The existence of a large scale recirculation region in the nearfield is
a common feature of the experiments described by Alpinieri (Ref. 8) and the
observed behavior of a pool fire. Thus the original eddy viscosity model
described by Eq. (11) was replaced by the expression

$$\rho \varepsilon_{vg} = k_z \, r_{1/2} \, \rho_e \, (u_c + k_v/u_e) \qquad (12)$$

where k_v has been used to replace the term u_e^2 in Alpinieri's expression, and taken to be 1.0. k_z is an adjustable eddy viscosity coefficient; as was the case for the viscosity model given by Eq. (11), the values of this coefficient may be different in different regions of the flow. For the particular case of the pool fire, for which the initial velocity u_0 is of the order of 0.025 m/sec (0.08 ft/sec), the bracketed velocity term in Eq. (12) is initially of the order of $1/u_0$, compared to a direct u_0 proportionality expressed by Eq. (11). As the computation continues, u_c, driven by buoyancy effects, increases to 20-30 m/sec (66-98 ft/sec), so that the bracketed term becomes of the order of $1.5 \, u_c$. Thus the effect of the use of this model is to provide a substantially greater eddy viscosity level early in the fire computation than would be achieved by the more conventional approach embodied in Eq. (11).

Results of the use of the Alpinieri formulation, Eq. (12) are compared with the results obtained using Eq. (11) and the experimental data for the 15 m (50 ft) fire on Fig. 2. Computations with the Alpinieri model using two sets of viscosity coefficients are shown. It can be seen from this comparison that both the early (low altitude, h) and late (high altitude) results are considerably improved through the use of the Alpinieri model; the changeover between coefficient values in each of the Alpinieri model computations occurs at $h = r_p$ (7.5 m). This improvement in the predictions for the pool fire is not an endorsement of the use of the Alpinieri approach in general, but these results indicate that strictly from the standpoint of the use of the eddy viscosity model in conjunction with a parabolic analysis as a correlative tool, an improved correlation can be obtained.

The results shown in Fig. 2 also show that the overall centerline temperature profile prediction is poor in the region of maximum temperature. Temperatures near to the adiabatic flame temperature are predicted to occur along the flow field centerline, but nowhere in the flame did measured temperatures approach this limit. Since the temperatures were measured using unshielded thermocouples, some error is inherent in the experimental results, but this error could not explain the 700-800°K discrepancy observed. Further, gas sample data indicated considerable unburned hydrocarbons in the region where maximum gas phase temperatures are predicted. Both of these observations

16

indicate that the effects of chemical kinetics and a large-scale unmixedness are of importance in the pool flame development process.

2.3 CHEMISTRY MODELING

Because the objective of the pool fire modeling work described in this report was to obtain a computation of the structural details of the fire that are important to the prediction of carbon fiber transport and consumption, the basic model formulation requires an accurate definition of the thermal field rather than the details of the chemical species. Thus the selection of a chemical system in terms of the number and kind of species considered can be somewhat arbitrary.

In a hydrocarbon-air system the principal products of combustion are H_2O and CO_2; for fuel-lean conditions O_2 will remain while in the fuel-rich regime unburned fuel will be found with the products of combustion. Dissociation of the major species at high temperatures results in the presence of H, O, OH, and CO in the fuel lean region, while under fuel rich conditions even more species, including a variety of hydrocarbon fragments and soot, will appear. At temperatures above about 2500°K the dissociation of nitrogen will begin to become significant.

All of these species can be included in an equilibrium chemistry computation and many of them have also been included in finite rate chemistry models (although considerable work is still required to establish usable finite rate chemistry models for complex fuels under fuel-rich conditions). However, both full-equilibrium and finite-rate chemical kinetics models require considerable computational time and involve a level of computational complexity that is not warranted given the objectives of the pool fire calculation. Instead, as cited above, the principal quantity of interest in the pool fire calculation is the temperature, and it has been demonstrated by Edelman et al. (Ref. 9) that accurate temperature predictions, for temperatures ≤ 2500°K, can be obtained using a simple quasi-complete equilibrium formulation. This is demonstrated by the results shown on Fig. 3, from Ref. [9], in which the temperatures predicted by the quasi-complete equilibrium model are compared with those obtained with a full equilibrium formulation, for a propane-air system. Good agreement can be seen except near stoichiometric and at the higher equivalence ratios.
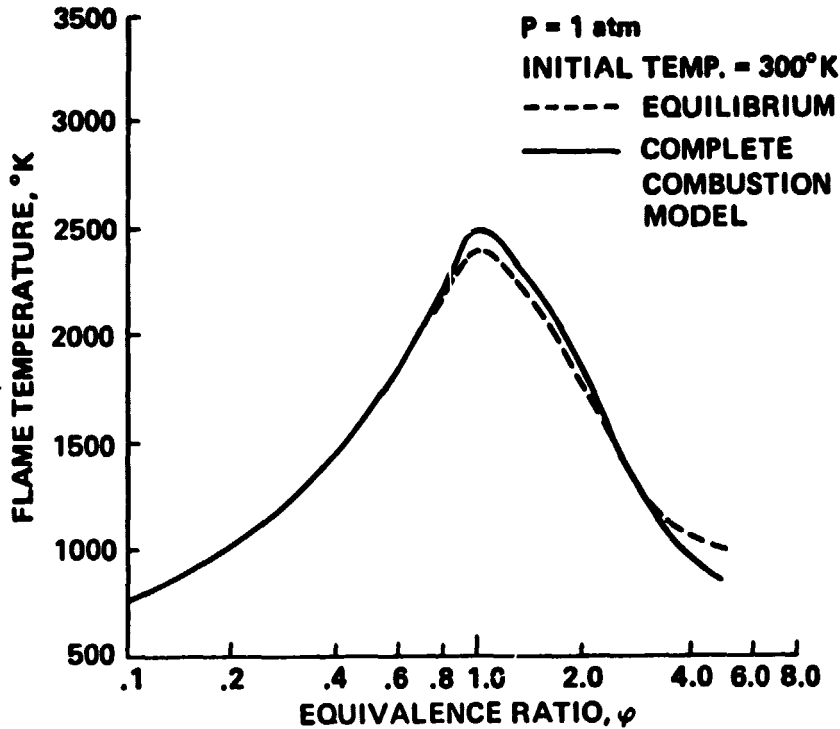
FIGURE 3. Comparison of Quasi-Complete Combustion Model with
Equilibrium Chemistry for a Propane-Air System.

In the form used in the pool fire model, the spectrum of equivalence
ratios encountered in the fire is divided into distinct regimes, defined by
the fuel/oxygen ratio; for fuel rich regions, a temperature limit is also
used to define regions in which soot is produced. For the fuel-lean regime,
complete oxidation of the fuel to the products CO_2 and H_2O is assumed to
occur. The upper limit for this regime is the stoichiometric point where the
atom balance is given by

$$\frac{1}{2} \tilde{\alpha}_H + 2\tilde{\alpha}_C = \tilde{\alpha}_O \tag{13}$$

in which the $\tilde{\alpha}$'s are the element molar concentrations. In terms of element
mass fractions, this relationship can be written

$$\frac{1}{2} \frac{\tilde{\beta}_H}{W_H} + 2 \frac{\tilde{\beta}_C}{W_C} = \frac{\tilde{\beta}_O}{W_O} \tag{14}$$

18

Accordingly, the lean regime is defined within the limits

$$\frac{\tilde{\beta}_O}{W_O} \geq \frac{1}{2}\frac{\tilde{\beta}_H}{W_H} + 2\frac{\tilde{\beta}_C}{W_C} \geq 0 \tag{15}$$

and the specie mass fractions are given by

$$\beta_{H_2O} = \frac{1}{2}\tilde{\beta}_H \frac{W_{H_2O}}{W_H} \tag{16}$$

$$\beta_{CO_2} = \tilde{\beta}_C \frac{W_{CO_2}}{W_C} \tag{17}$$

$$\beta_{O_2} = W_{O_2}\left[\frac{1}{2}\frac{\tilde{\beta}_O}{W_O} - \frac{1}{4}\frac{\tilde{\beta}_H}{W_H} - \frac{\tilde{\beta}_C}{W_C}\right] \tag{18}$$

In the fuel rich region, pure fuel remains if the local temperature is below 750°K; for temperatures above 750°K, soot can be formed. The fuel-rich region is itself divided into two zones. For fuel-oxygen ratios just above stoichiometric, the fuel is assumed to be oxidized to CO and CO_2, while the molar concentration of water remains essentially constant. Thus, for

$$2\frac{\tilde{\beta}_C}{W_C} + \frac{1}{2}\frac{\tilde{\beta}_H}{W_H} > \frac{\tilde{\beta}_O}{W_O} \geq \frac{\tilde{\beta}_C}{W_C} + \frac{1}{2}\frac{\tilde{\beta}_H}{W_H} \tag{19}$$

the species mass fractions are given by

$$\beta_{H_2O} = \frac{1}{2}\tilde{\beta}_H \frac{W_{H_2O}}{W_H} \tag{20}$$

$$\beta_{CO} = W_{CO}\left[2\frac{\tilde{\beta}_C}{W_C} - \frac{\tilde{\beta}_O}{W_O} + \frac{1}{2}\frac{\tilde{\beta}_H}{W_H}\right] \tag{21}$$

$$\beta_{CO_2} = W_{CO_2}\left[\frac{\tilde{\beta}_O}{W_O} - \frac{1}{2}\frac{\tilde{\beta}_H}{W_H} - \frac{\tilde{\beta}_C}{W_C}\right] \tag{22}$$

In the next region,

$$\Rightarrow \quad \frac{\tilde{\beta}_C}{W_C} + \frac{1}{2}\frac{\tilde{\beta}_H}{W_H} > \frac{\tilde{\beta}_O}{W_O} \tag{23}$$

a further subdivision is defined depending on the temperature and the carbon/ oxygen atom mole ratio. Thus, for $T < 750°K$ and $\tilde{\beta}_C/W_C < \dfrac{\tilde{\beta}_O}{W_O}$, the products are assumed to be H_2, CO_2, and fuel ($C_n H_m$), so that

$$\beta_{H_2} = \frac{W_{H_2}}{2}\left[\frac{\tilde{\beta}_H}{W_H} - \frac{m}{n}\left(\frac{\tilde{\beta}_C}{W_C} - \frac{1}{2}\frac{\tilde{\beta}_O}{W_O}\right)\right] \tag{24}$$

$$\beta_{CO_2} = \frac{1}{2}\tilde{\beta}_O\,\frac{W_{CO_2}}{W_O} \tag{25}$$

and

$$\beta_{C_n H_m} = \frac{W_{C_n H_m}}{n}\left[\frac{\tilde{\beta}_C}{W_C} - \frac{1}{2}\frac{\tilde{\beta}_O}{W_O}\right] \tag{26}$$

while for $T < 750°K$ and $\tilde{\beta}_C/W_C > \tilde{\beta}_O/W_O$, the products are assumed to be H_2, CO, and $C_n H_m$, and

$$\beta_{H_2} = \frac{W_{H_2}}{2}\left[\frac{\tilde{\beta}_H}{W_H} - \frac{m}{n}\left(\frac{\tilde{\beta}_C}{W_C} - \frac{\tilde{\beta}_O}{W_O}\right)\right] \tag{27}$$

$$\beta_{CO} = \frac{W_{CO}}{W_O}\tilde{\beta}_O \tag{28}$$

and

$$\beta_{C_n H_m} = \frac{W_{C_n H_m}}{n}\left[\frac{\tilde{\beta}_C}{W_C} - \frac{\tilde{\beta}_O}{W_O}\right] \tag{29}$$

If the temperature is above $750°K$, and $\tilde{\beta}_O/W_O > \tilde{\beta}_C/W_C$, it is assumed that the fuel decomposes and partially oxidizes to CO, H_2, and H_2O, so that

$$\beta_{CO} = \frac{W_{CO}}{W_C}\tilde{\beta}_C \tag{30}$$

$$\beta_{H_2} = W_{H_2}\left[\frac{\tilde{\beta}_C}{W_C} + \frac{1}{2}\frac{\tilde{\beta}_H}{W_H} - \frac{\tilde{\beta}_O}{W_O}\right] \tag{31}$$

$$\beta_{H_2O} = W_{H_2O} \frac{\tilde{\beta}_O}{W_O} - \frac{\tilde{\beta}_C}{W_C} \tag{32}$$

while, if $T > 750°K$ and $\tilde{\beta}_C/W_C > \tilde{\beta}_O/W_O$, soot is formed:

$$\beta_{C(s)} = \tilde{\beta}_C - \frac{W_C}{W_O} \tilde{\beta}_O \tag{33}$$

$$\beta_{CO} = \frac{W_{CO}}{W_O} \tilde{\beta}_O \tag{34}$$

and

$$\dot{\beta}_{H_2} = 2 \frac{W_{H_2}}{W_H} \tilde{\beta}_H \tag{35}$$

Since nitrogen is assumed not to react, it satisfies the relationship

$$\beta_{N_2} = \tilde{\beta}_N \tag{36}$$

throughout the flow.

Note that when solid carbon (soot) is formed, it becomes a particulate phase specie and thus enters the particle tracking methodology to be described subsequently in this section. It may also be consumed in its subsequent passage through the fire, producing CO_2; the rate for this conversion is given by the expression obtained by Lee, Thring and Beer [10]

$$\frac{1}{\pi d_j^2} \frac{dm_j}{dt} = 1.085 \times 10^4 \frac{P_{O_2}}{T} \exp(-39,300/RT) \tag{37}$$

in which d_j and m_j are the mean diameter and mass of the jth particle class, P_{O_2} and T are the local oxygen partial pressure and temperature, in atmospheres and degrees Kelvin, respectively, and R is the universal gas constant in units of cal/g-mole °K.

Given this chemistry formulation, the computation proceeds in the following manner: Transport equations are written for the four gas-phase elements H, O, C, and N, and for each of ten particulate-phase "species,"

which constitute two classes of soot particles and eight of carbon fibers. Solution of these equations, along with the momentum and energy equations yields the gas-phase elements at each point, and the chemistry model given by Eqs. (19)-(36) yields the species taken to exist at a given point in the flow. With the gas-phase species defined along with the local enthalpy level, a temperature is obtained using Eq. (7). If soot is formed, the appropriate mass fraction is deleted from the gas-phase carbon element and added to the appropriate particle class. Under a thermal equilibrium assumption the particulate species are taken to be at the same temperature as the gas phase, so that this temperature is used to compute the particulate consumption rate for each species and the thermal radiation from the particulate species, both of which will be discussed further in subsequent sections of this report. The results of the consumption process represent a source term for the gas-phase carbon element for the next step in the computation.

Although the chemistry modeling approach outlined in this section was reasonably successful in the flame computations described in Ref. 9, the results displayed in Fig 2 indicated several unsatisfactory features of the model. One of these is the underprediction of the temperatures observed at the centerline in the early part of the fire, and the second is the strong overprediction of peak centerline temperature. The underprediction of the temperature in the early part of the fire can be traced in part at least to the chemistry model itself: as seen on Fig. 3, for equivalence ratios greater than about three the basic model of Ref. 9 strongly underpredicts the temperature for a propane-air mixture. Both measurements and computational results show very fuel-rich equivalence ratios at the centerline for h < 4m, with measured equivalence ratios of 10-20 being observed. On the other hand, the overpredicted peak temperature is due to the prediction of stoichiometric conditions along the fire centerline: with the basic chemistry model temperatures close to the adiabatic flame temperature will be predicted at $\phi = 1$. Since temperatures this high were never measured within the pool fire, it is evident that other factors were involved in the experiments which resulted in the temperature levels observed.

Thus the comparison of computational results with experimental data such as depicted on Fig. 2 dictated further modifications to the basic chemistry model. These modifications took two forms. In view of the results shown on

22

Fig. 3, and of other computations, the basic chemistry formulation was modified to incorporate a partial-equilibrium expression for the species CO, CO_2, and C in very fuel-rich regions. Examination of these and other results and observation of the behavior of the pool fire plume during the experimental program indicated that there were large-scale unmixedness effects, i.e., that although on the average local fuel-air ratios near stoichiometric were seen, this average was made up of the sequential passage of fuel-rich and fuel-lean elements, so that the average fuel-air ratio did not adequately describe the actual flow. To incorporate this phenomenon, an unmixedness model was developed and applied to the calculation.

2.3.1 Partial Equilibrium for Fuel-Rich Regions

The chemistry model modification introduced in the fuel-rich region, for $\tilde{\beta}_C/\tilde{\beta}_O > 1$ and $T > 750°K$ involves the use of the so-called Boudonard reaction (Ref. 11)

$$CO \rightleftarrows \frac{1}{2} CO_2 + \frac{1}{2} C(S) \tag{38}$$

as a partial equilibrium relationship. The equilibrium constant for the Boudouard reaction is

$$K_p^B = [P_{CO}]^2/P_{CO_2} \tag{39}$$

and values of K_p^B are quoted in Ref. 11 and given below:

T°K	K_p^B	T°K	K_p^B	T°K	K_p^B
300	1.63×10^{-21}	900	0.195	1750	1.06×10^4
500	1.82×10^{-9}	1000	1.91	2000	4.21×10^4
700	2.71×10^{-4}	1400	628	3000	2.8×10^4

For application in the fire code, these equilibrium constant values were curve fit by the expression

$$\ln K_p^B = 20.649 - 2.0002 \times 10^4/T \tag{40}$$

and the soot concentration was computed using this equilibrium constant rather than through an arbitrary specification of the levels of CO, CO_2 and soot. Note that Eq. (40) requires the local temperature: since this is a function, given the enthalpy, of the species distribution, the Boudard equilibrium is computed iteratively in the fire model.

2.3.2 Turbulent Unmixedness Modeling

In the simple approach adopted for this effort, it is assumed that because of unmixedness a portion of the total oxygen and fuel at each point in the flow is unavailable for reaction, and that the fraction unavailable can be realated to the local velocity fluctuation level. The proportion of fuel unavailable is taken to be related to the unavailable oxygen by the local stoichiometry. Thus, although local $\phi=1$ will still be observed, the temperature computed for this point will be modified by the dilution of the products of combustion by the amount of oxygen and fuel deemed to remain unburned.

Therefore, it is assumed that

$$\tilde{\beta}_{O_2}\Big|_u = fr \cdot \tilde{\beta}_{O_2}\Big|_t \tag{41}$$

where "u" and "t" refer to "unburned" and "total" respectively, and

$$fr \propto \frac{u'}{u} \tag{42}$$

Then, assuming that $\frac{u'}{u}$ is related to the local turbulent kinetic energy level,

$$\frac{u'}{u} \propto \frac{e}{u^2}^{1/2} \tag{43}$$

and noting that, consistent with the use of a locally dependent eddy viscosity model, the turbulent energy production can be equated to the turbulence energy dissipation:

$$\rho \frac{a_2 e^{3/2}}{\ell_K} = \mu_T \left(\frac{\partial u}{\partial r}\right)^2 \tag{44}$$

a relationship for fr can be obtained:

$$fr = f \cdot \frac{\mu_T \ell_K}{\rho}^{1/3} \frac{\partial u}{\partial r}^{2/3}$$

(45)

where μ_T is the local turbulent viscosity, ℓ_K a length scale taken to be that used to obtain the local turbulent viscosity, ρ is the local density, and f a coefficient which is to be evaluated through comparison of predictions with data.

2.3.3 Effect of Chemistry Model Modifications

Of the two model modifications discussed in the preceding sections, the unmixedness formulation has by far the greatest effect. This is because the Boudouard equilibrium model is effective in only a very·limited region of the fire plume, near ground level. Because of the massive entrainment of air near the ground level in the calculated plume, the predicted fuel-air equivalence ratio along the axis quickly drops to a level at which the Boudonard equilibrium relationship provides only a marginal difference in calculated temperature from that obtained using the basic chemistry model.

On the other hand, the unmixedness formulation has a strong impact on the predicted plume centerline temperature development, as is shown in Fig. 4. Results for two levels of unmixedness are shown on this figure, in comparison with the previously presented results for no unmixedness and with the experimental data for the 15 meter (50 foot) diameter fire. The major impact of the unmixednesness model is to drastically reduce the predicted peak temperature along the centerline: in the calculations shown on Fig. 4 this reduction amounts to more than 700°K for the model with f = 0.75 (see Eq. 45) compared to without the unmixedness correction (i.e., f=0). In all computations shown on Fig. 4, the same eddy viscosity model and value of the emissivity in the radiation model (Section 2.4) has been used. Noted that the incorporation of the unmixedness effect also changes the shape of the predicted temperature curve, particularly at heights below about four meters. This is because the low temperatures generated though the incorporation of unmixedness alter the bouyancy and thus alter the overall plume flowfield development. The initial entrainment of ambient air is driven by the assumed initial velocity of the fuel, and is constant for all of the cases shown, but from this point on the mixing process is driven by the buoyancy term which depends directly on the predicted temperature level. Since this in turn affects the local velocity
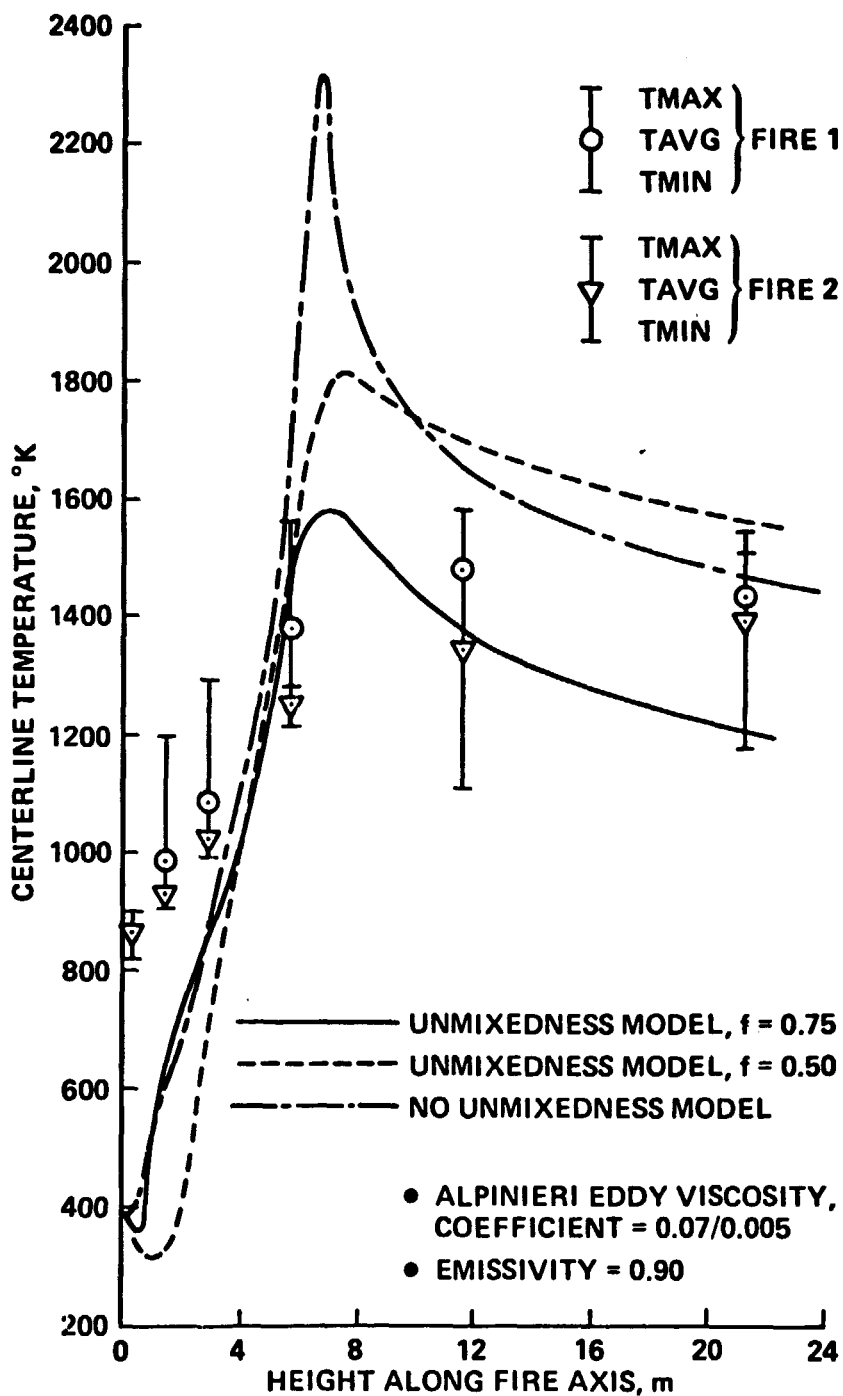
25

FIGURE 4. Effect of Incorporation of Unmixedness Model On
Predicted Centerline Temperature Distribution

gradient, and thus, through Eq. (45) the computed unmixedness, the effect
of unmixedness on the plume centerline temperature is not a linear function
of the degree of unmixedness, as these results clearly show.

2.4 PLUME RADIATION MODEL

Radiation from the fire plume to the surroundings can be a significant
source of energy loss from the plume. In order to account for this loss,
represented by the term q_r in Eq. (5), the radiation from the plume has been
computed for the optically thin limit.

In the optically thin limit, the monochromatic radiant energy loss term
can be written

$$\frac{dq_{r\lambda}}{dr} = 4 \, k_\lambda \, e_{b\lambda}(r) \tag{46}$$

(Ref. 12) in which $e_{b\lambda}$ is given by Planck's law and k_λ is the monochromatic
volumetric absorption coefficient. The term $e_{b\lambda}$, which is a function of the
local temperature, has been written as a function of radius since in the plume
$T = T(r)$.

For the present work, Eq. (46) has been used in the form of an average
(over wave number) of the expression given with $k \simeq 0.25$. Since the parti-
culate phase carbon is the most important radiation contributor in the fire,
gas phase emission has been ignored. Approaches similar to that outlined here
have been successfully applied to the prediction of carbon particle radiation
from rocket plumes (Ref. 13).

Although this approach is simple to apply, the optically thin limit is
not a good approximation to the behavior of the radiation flux in a dense,
sooty plume: under these circumstances the radiative transport involves
the absorption and re-emission of radiation from soot particles all along the
lines of sight within the plume. However, the optically thin model can be
used to gain some insights into the effects of radiation by variation in the
values assumed for the soot particle emissivity, where lower values of emis-
sivity account to some extent for the absorbing/emitting character of the actual
fire plume. The results of several computations, incorporating the unmixedness
correction described in Section 2.3, with $f = 0.5$, and using the Alpinieri

eddy viscosity model, Section 2.2, but varying the assumed particle-phase emissivity from 0 to 0.9 are shown on Fig. 5. These results indicate that neglecting radiation effects is not a feasible approach to the computation of the plume development, and that for all other effects constant, the predicted plume development is a strong function of the radiant energy loss. It is also of interest to note that at an emissivity of 0.5, the total radiant energy loss is about 20% of the total energy produced by the consumption of the fuel, which is essentially the proportion of radiant energy/total energy observed in laboratory scale pool fires.

2.5 PARTICULATE TRANSPORT MODELING

Since the basic objective of the development of the fire plume model described in this report was to provide a means for the computation of the transport and consumption of graphite fibers released during a pool fire, a particulate tracking methodology is a required feature. This particle tracking model is also used to compute the transport of soot particles within the fire plume.

The combined effects of continuous reaction of both fibers and soot and the non-uniform velocity and temperature fields within the fire plume provide conditions resulting in a spectrum of particle sizes at every point in the flow. To completely specify the particle reaction rate and the production of gas phase species from the consumption of the soot and fibers, the local particle size and number density distribution must be known. This in turn requires the development of a methodology for tracking the particle history throughout the flow.

The track the particle history through the flow, the total amount of particulate material present at every point in the field is divided into a set of categories. These categories can be based on any parameter which can be used to differentiate particles: for the fire application particle size (diameter for the assumed spherical soot particles and length for the fibers) is the relevant parameter. Thus categories are set up by dividing the total range of particle sizes into classes defined by a minimum and a maximum particle size.
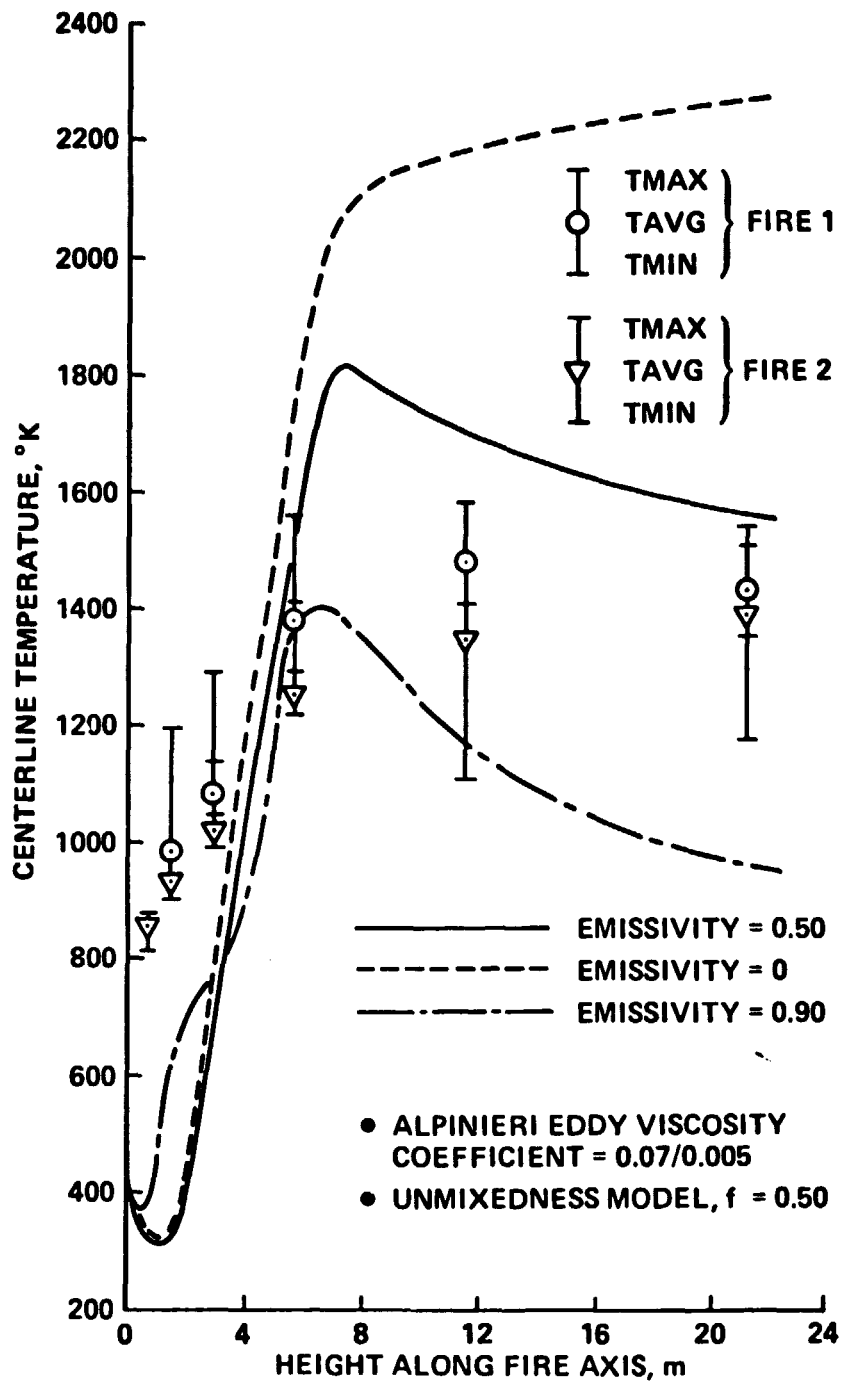
FIGURE 5. Effect of Radiation Heat Flux on Predicted
Centerline Temperature Distribution

Consider, for simplicity, spherical particles. Within each size range, all particles are combined to form an average with a volume to surface area ratio equal to that of the summation over all contributions. This equivalent particle size is the Sauter mean value and is expressed as

$$r_s = \sum n_i r_i^3 / \sum n_i r_i^2 \tag{47}$$

where n_i particles have radius r_i. The mass fraction of each category is equal to the sum of the mass fractions of each contribution. With the average size of category particles and the total category mass fraction known, the appropriate number of equivalent particles is established for every class. This representation provides an exact equivalence for the subsequent rate process provided the rate of change of mass depends directly upon the particle surface area.

The particle distribution array in terms of size, mass fraction, and number in each category at every grip point can only be altered by changes in size of the particle due to chemical reaction and by diffusion of particles from the neighboring flow. The radius of the particle changes in accordance with the particle consumption expression as the flowfield develops. Thus, after every step, the new particle size is given by

$$r = r_0 + \int_{xo}^{x} \frac{dr}{dx} \Delta x \tag{48}$$

After every step the updated radius array must be reclassified in order to account for the transition of particles from one category to another. Since it is possible for more than one contribution to be made to a particular category, the total category mass must then be reaveraged using the Sauter criteria, to establish the proper radius and number for the group. The particle array in terms of mass fraction, size and number density resulting from the kinetics of the combustion process will be defined as:

$$
\begin{array}{l}
G(J,I)_k \\
R(J,I)_k \quad \text{at grid point} \begin{pmatrix} n+1 \\ m \end{pmatrix} \\
N(J,I)_k
\end{array}
$$

Each category in the particle array is altered by the diffusion of particles of the same category from neighboring upstream locations. Subdividing the particle mass fraction α_i into each separate category and treating the category mass fractions as separate species, the diffusion equation can be written in finite difference form in von Mises coordinates as

$$\alpha_{i,n+1,m} = \alpha_{i,n,m} + \Delta x \left(\frac{Wi}{u}\right)_{n,m} + \frac{\Delta}{\psi^N (\Delta\psi)^2} \left\{ \left(\frac{b}{Sc}_{n,m+1/2}\right) \alpha_{i,n,m+1} \right. $$

$$\left. \left[\left(\frac{b}{Sc}\right)_{n,m+1/2} + \left(\frac{b}{Sc}\right)_{n,m+1/2}\right] \alpha_{i,n,m} + \left(\frac{b}{Sc}\right)_{n,m-1/2} \alpha_{i,n,m-1} \right\} \quad (49)$$

where the n,m subscripts refer to the grip point locations shown in Fig. 6.

The second term in Eq. (49) represents the change in α_i due to the kinetics process as the flow moves downstream from n to n+1. The sum of the first two terms is the total mass fraction of category particles present downstream due to kinetic processes, and the remaining term represents the contribution to the mass fraction from diffusion. Noting Fig. 6, the diffusional term can be split into the contributions from each of the three upstream points:

$$\Delta G_1 = \frac{\Delta x}{\psi^N (\Delta\psi)^2} \left(\frac{b}{Sc}\right)_{n,m+1/2} \alpha_{i,n,m+1} \quad (50)$$

$$\Delta G_2 = -\frac{\Delta x}{\psi^N (\Delta\psi)^2} \left[\left(\frac{b}{Sc}\right)_{n,m+1/2} + \left(\frac{b}{Sc}\right)_{n,m-1/2}\right] \alpha_{i,n,m} \quad (51)$$

$$\Delta G_3 = \frac{\Delta x}{\psi^N (\Delta\psi)^2} \left(\frac{b}{Sc}\right)_{n,m-1/2} \alpha_{i,n,m-1} \quad (52)$$

For each of the categories present at a given grid point, we may express the category mass fraction as

$$G(J,I)_{n+1,m} = \left[\Delta x \left(\frac{Wi}{u}\right)\right]_{n,m} + \Delta G_1 + \Delta G_2 + \Delta G_3 \quad (53)$$

where the kinetics contribution is evaluated as $G(J,I)_k$ with its associated $R(J,I)_k$ and $N(J,I)_k$. Knowing the category sizes associated with each upstream
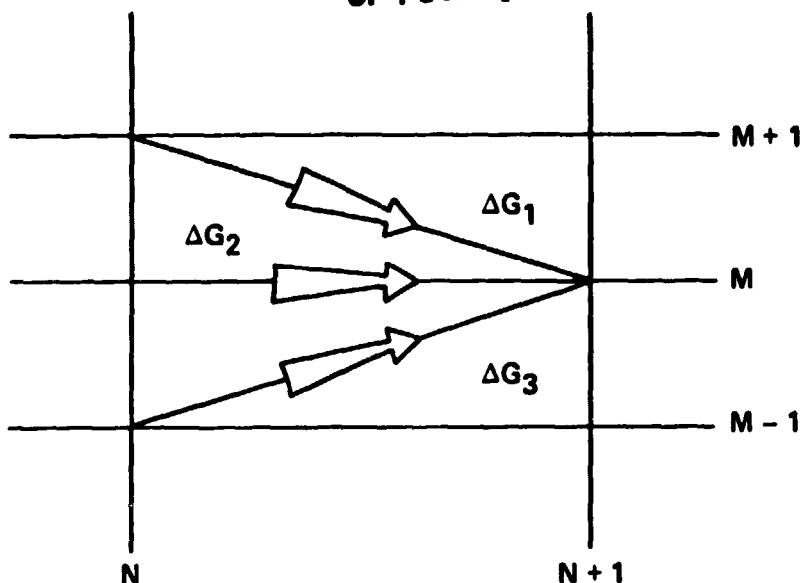
FIGURE 6. Finite-Difference Grid System.

contribution the Sauter criteria (or other appropriate characterization cri-
teria) can be used to define the new category radius:

$R(J,I)n+1,m =$

$$\frac{G(J,I)k + \Delta G_1 + \Delta G_2 + \Delta G_3}{\dfrac{G(J,I)k}{R(J,I)k} + \dfrac{\Delta G_1}{R(J,I)n,m+1} + \dfrac{\Delta G_1}{R(J,I)n,m} + \dfrac{\Delta G_3}{R(J,I)n,m-1}} \tag{54}$$

Knowing the new mass fraction and size, the number density of particles is
determined from:

$$N(J,I)n+1,m = \frac{\rho n+1,m G(J,I)n+1,m}{4/3\pi\rho_L R(J,I)n+1,m} \tag{55}$$

2.5.1 Effect of Source Location

A variable of interest with respect to the distribution and consumption of
fibers in the fire is the effect of the ground level location of the fibers
within the pool. To investigate the effects of source location, the nonuniform,

but axisymmetric fiber source locations shown in Fig. 7 were used as initial conditions for a 30 meter fire calculation. In all cases the total fiber flow rate (10 kg/min) was the same, but for one computation the fiber source was assumed to be a centrally-located disc, while in the other case an annular ring source was used.*

The results of these computations are shown in Figs. 8(a) - 8(c), compared to the results of a uniform fiber distribution calculation. Although some differences in detail are apparent in these figures, it is clear that overall the differences are small and would be insignificant in the computation of the subsequent atmospheric dispersion process.

Some insight into the reasons for the insensitivity of the results to the initial particle source location can be gained from the isotherm and stream function profiles shown in Fig. 9. The isotherm profiles shown a strong "necking down" in the early part of the calculation, the reasons for which are made apparent in the stream function plot. Since the stream function is proportional to the square root of the mass flow in the plume, it can be seen that the vast bulk of the flow at the top of the plume results from the massive entrainment of air generated by the large buoyancy-driven accelerations in the fire. Indeed, the $\psi/\psi = 1$ stream function, which represents the mass that originates within the pool, is very quickly driven to the centerline of the flowfield by the air entrainment. Thus material originating in the pool, whatever its location, is quickly driven in towards the centerline, limiting the overall effects of source location. The differences observed between source location results in Figs. 8(a) - 8(c) are primarily a result of different turbulent diffusion rates developed as a result of the different initial distributions.

---

* These computations, originally described in Ref. 3, utilize a fire plume model which does not incorporate the unmixedness effects described in Section 2.2. However, differences in fire plume structure observed with the incorporation of unmixedness would not materially change the results described in this subsection.
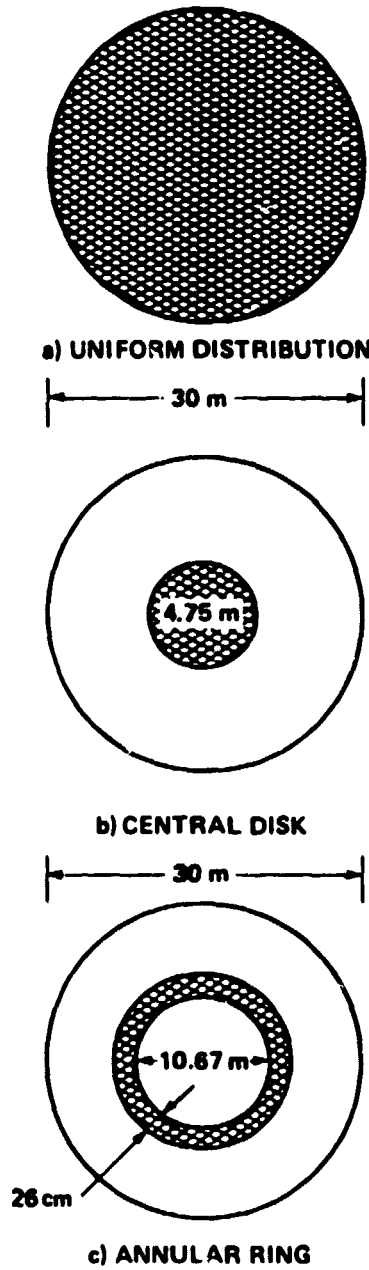
FIBER SOURCE LOCATION SHOWN CROSS-HATCHED

a) UNIFORM DISTRIBUTION

30 m

b) CENTRAL DISK

30 m

c) ANNULAR RING

FIGURE 7.   Fiber Source Locations

34

PARTICLE CLASS 3   PARTICLE RADIUS = 24μ

——— = UNIFORM

- - - - = ANNULAR RING

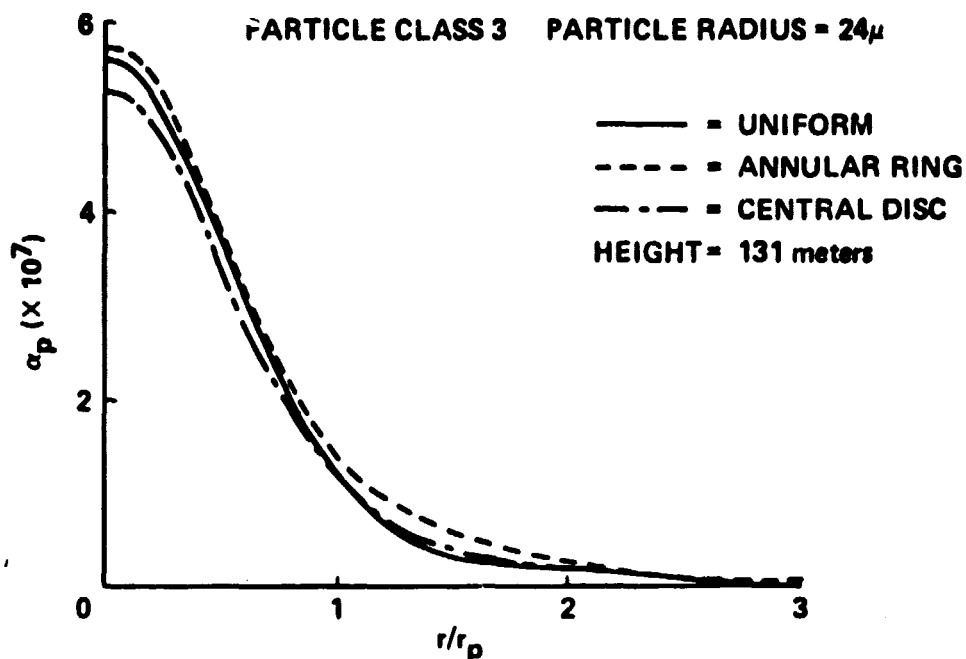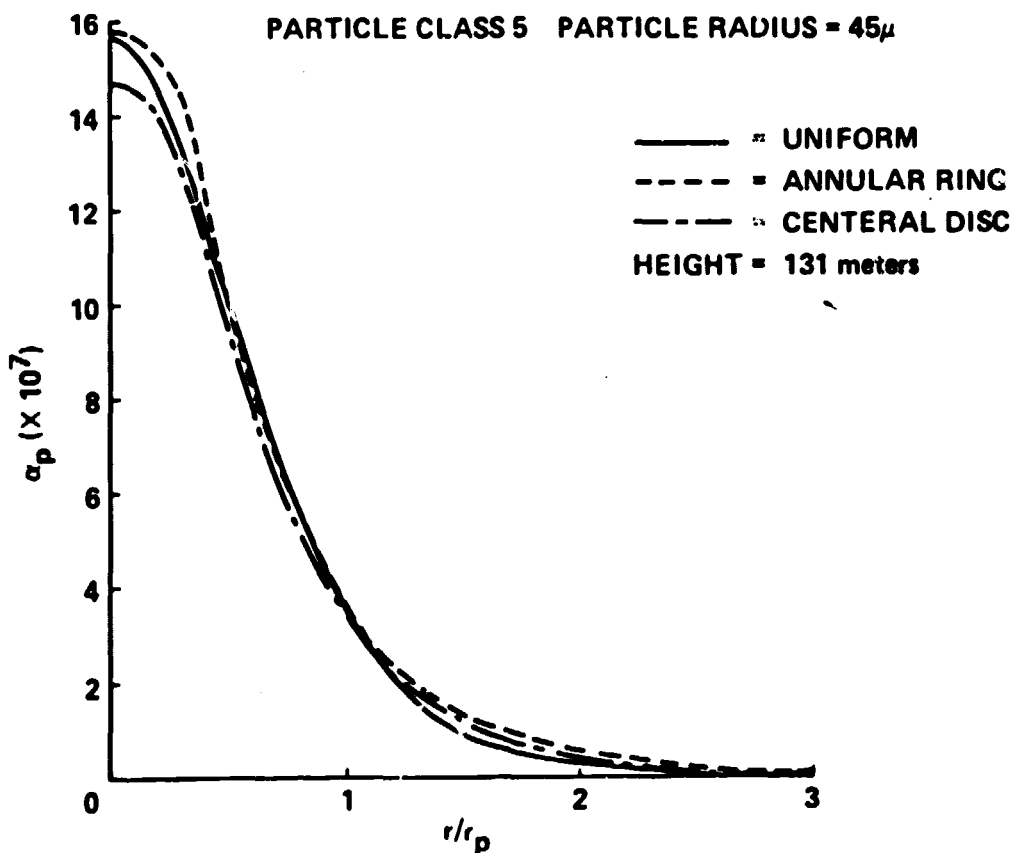— · — = CENTRAL DISC

HEIGHT = 131 meters

$\alpha_p \ (\times 10^7)$

r/r_p

FIGURE 8(a).   Effect of Source Location on Distribution of Particulates
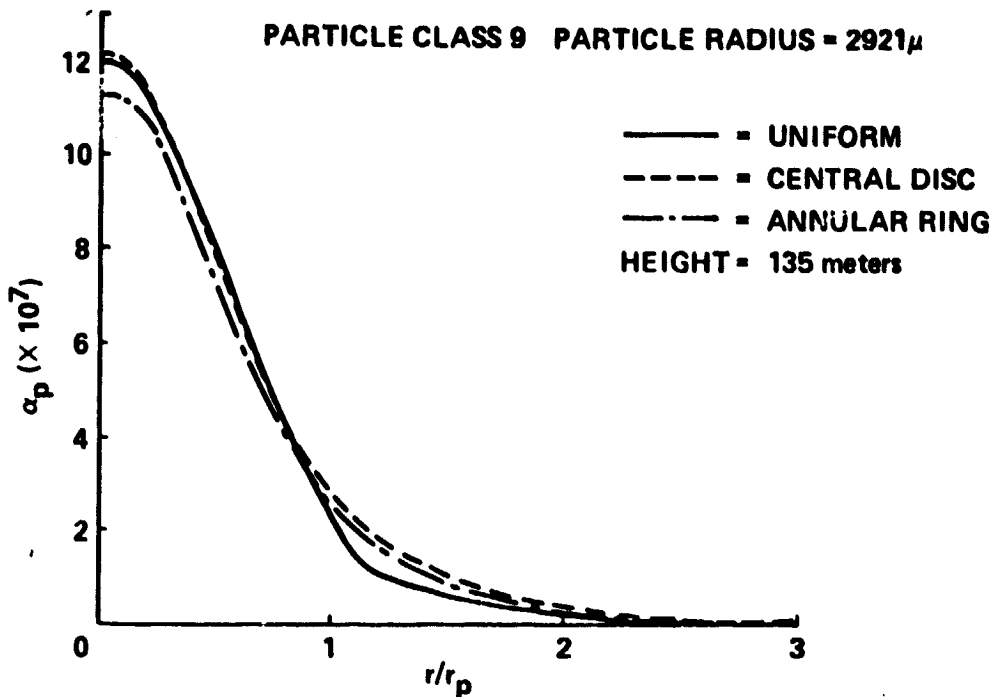at End of Fire Calculation - Single Fibers

PARTICLE CLASS 5   PARTICLE RADIUS = 45μ

——— = UNIFORM

- - - - = ANNULAR RING

— · — = CENTERAL DISC

HEIGHT = 131 meters

$\alpha_p \ (\times 10^7)$

r/r_p

FIGURE 8(b).   Effect of Source Location on Distribution of Particulates
at End of Fire Calculation - Single Fibers

FIGURE 8(c).   Effect of Source Location on Distribution of Particulates
at End of Fire Calculation - Fiber Clusters

2.6 FIBER CONSUMPTION MODEL

The Lee, Thring and Beer model (Ref. 10) for the consumption of soot
particles was utilized in the fire modeling described in Ref. 3 to predict
fiber consumption rates. In this work, the fiber consumption model has been
modified to reflect the results of work done at NASA-Langley on individual fiber
consumption rates as a function of temperature and oxygen partial pressure.
However, only one set of data, for a temperature range of 450°C to 700°C
and an oxygen partial pressure of 0.0816 atm was suitable for the development
of a fiber oxidation rate expression. Thus, while a modified rate expression
was developed from these data as shown on Fig. 10, it can only be considered
to be preliminary as the possibly substantial effect of oxygen partial pressure
on the rate has not been determined. Further, the experiments involve a
variable particle heat up time during which some consumption is occurring.
This variable heat up time cannot be incorporated into the development of
the model for particle consumption. Finally, possible physical differences
(e.g., surface coatings) between the test particles and those released in a fire
have not been investigated. All of these uncertainities can lead to substan-
tial differences between predicted and measured particle consumption rates in
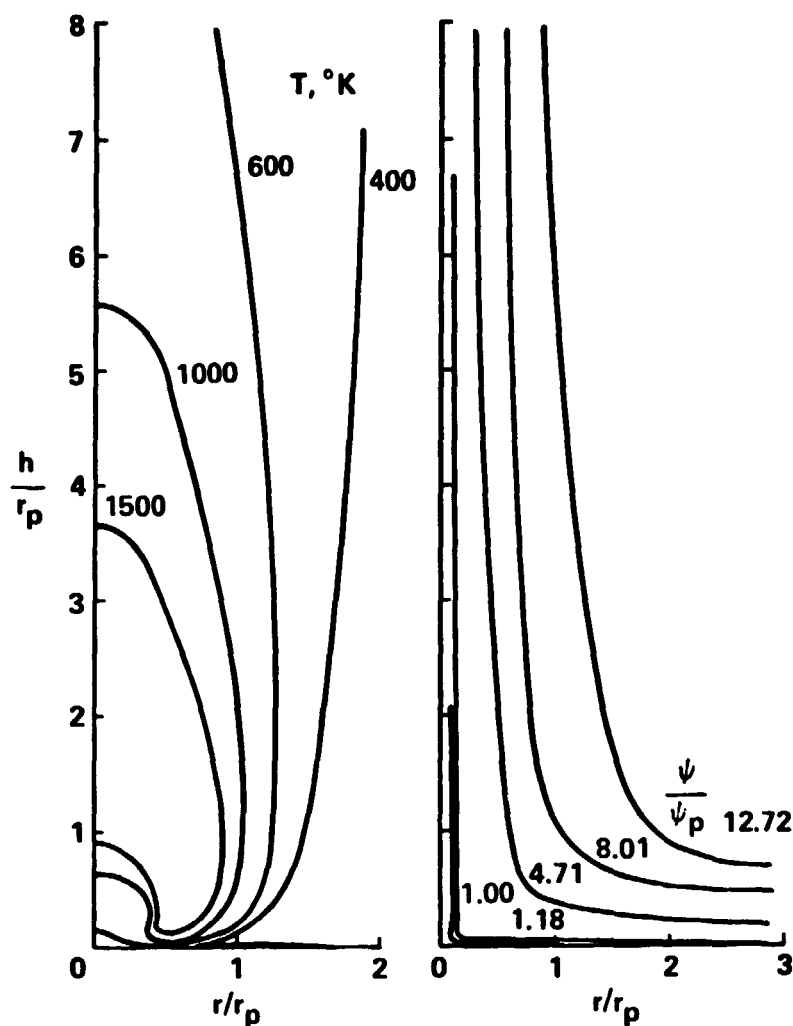a fire environment.

36

FIGURE 9.   Isotherm and Stream Function Profiles for 30m Fire

2.7   FIBER THERMAL NONEQUILIBRIUM

The computations reported in Ref. 3 were all carried out under the assumption of fiber thermal equilibrium, that is, that the fibers are everywhere the same temperature as the gas phase. This assumption can be relaxed, so that the heating and subsequent cooling of the fibers in response to the gas phase temperature change is computed. This is done by writing a particle-phase energy transport equation for each particle class, which includes as source terms expressions representing the heating of the particle by conduction from the gas phase, energy loss from the particle caused by radiation, and heating of the particle caused by surface combustion, all of the energy of which is assumed to be absorbed by the particle.

EXP. DATA @ P_{o2} = 0.0816 atm; DIAM = 7 (μ)

$$\text{OXID. RATE} = \frac{5.83 \times 10^1 P_{o2}}{T^{\frac{1}{2}}} \text{ EXP. (-23,500/RT)}$$

——— EXP. DATA

— — PREDICTION
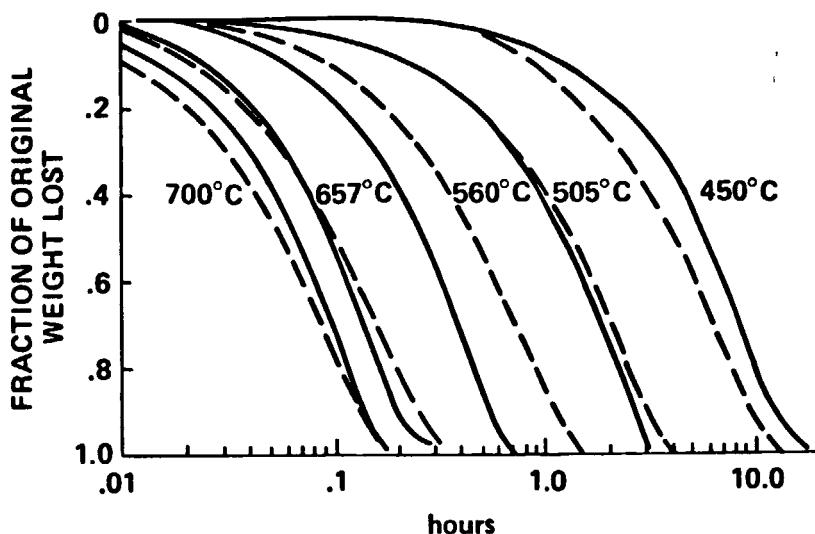
FIGURE 10.   Comparison of Modified Lee, Thring, and
Beer Model With Fiber Consumption Data.

To assess the need for the incorporation of a thermal nonequilibrium model, a number of one-dimensional single fiber computations were carried out which are of interest with regard to the response of the fibers to temperature changes and the effects of surface combustion on particle temperature. Fig. 11 depicts the response of a single fiber to gas-phase temperature change considering only conduction heat transfer (which is, however, the largest single contribution by a substantial amount). For this calculation, the initial gas-phase temperature (T_{go}) was 1500°K, and the initial fiber temperature (T_{p_o}) was 300°K. Under conduction-only conditions, and assuming that the particle specific heat and gas conductivity are constants, an analytical solution can be obtained; in the numerical solution both conductivity, λ, and heat capacity, C_{p_p}, are functions of the gas phase and particle temperatures, respectively. Fig. 11 shows that the 1/e response time of the fiber is about 0.10 seconds.

Within the fire, there may be regions of locally high (i.e., near stoichiometric) temperatures on scales of the order of 0.01 d_F, where d_F is the local fire diameter. If such high temperature regions exist, and a local fire diameter of the order of one-half the pool diameter is assumed, and it is further assumed that these eddies have a convection velocity relative to the mean velocity of the order of $0.1\bar{U}$, then a "hot" eddy lifetime is of the order of 0.03 seconds. Comparison of this lifetime with the single-fiber response time of 0.10 seconds indicates that the fibers are essentially unaffected by local temperature fluctuations.
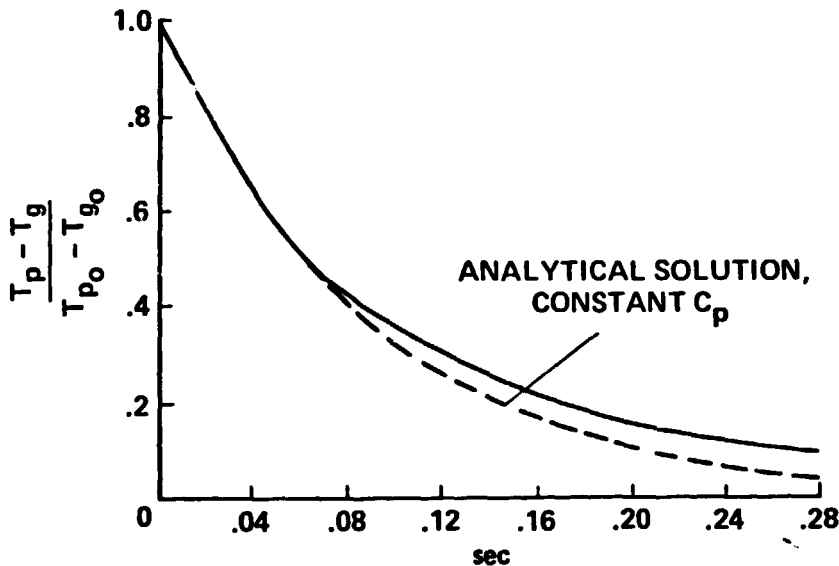
FIGURE 11.   Response of a Single Fiber to Gas-Phase Temperature,
$T_{p_0}-T_{g_0}$ = 1200°K, Conduction Only.

Additional one-dimensional calculation results including the effects of thermal radiation and particle consumption are shown in Fig. 12. As can be seen from this figure, the inclusion of radiation has a negligible effect on the temperature history; and the incorporation of particle combustion also leads, for these conditions, to negligible changes relative to the conduction only solution.
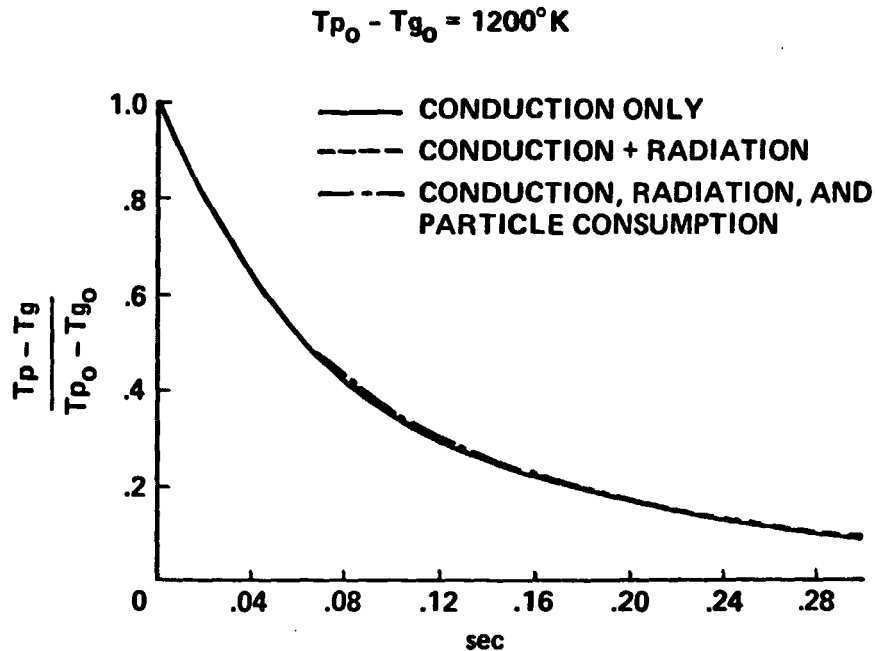
$Tp_0 - Tg_0 = 1200°K$

FIGURE 12.   Effects of Radiation and Particle Combustion
on Fiber Temperature History.

2.8 COMMENTS ON PARABOLIC MODELING OF LARGE POOL FIRES

It was pointed out in the introduction to this report that the modeling
of the open pool fire problem using the boundary layer form of the equations
of motion.   This approach was nevertheless adopted in order to use existing,
well-developed solution techniques, and because the information desired from
the model comprised fiber flux and distribution results in the region of the
fire in which the parabolic approximation is reasonable.   The applicability
of the parabolic formulation and be assessed at least in part by reference
the stream function plots shown on Fig. 9.   Under the parabolic assumption,
gradients in the dependent variables in the axial direction (i.e., vertically
along the plume axis) are assumed negligible compared to gradients in the
radial direction (i.e., horizontally).   The stream function contours shown on
Fig. 9 demonstrate that near ground level, this assumption is not met, and
axial gradients can be expected to be the same order of magnitude as (if not
larger than) the radial gradients.

The parabolic approach is thus an approximation to a complete fire model, and the errors inherent in the approximation cannot be evaluated without a more exact model for comparison. It is, however, clear that the major inaccuracies involved in a parabolic formulation of the pool fire problem are found at the lower levels of the fire, and it is in just this region that the major discrepancies between the computational results and the experimental data are observed. An "exact" formulation of the pool fire problem would involve the solution of the full Navier-Stokes equations, including axial diffusion and radial pressure gradients, but there are several obstacles that would have to be overcome to develop the more exact model.

Elliptic computations, such as an "exact" formulation of the pool fire problem, require the definition of boundary conditions on all of the boundaries of the problem. For the zero-wind pool fire, this means that boundary conditions must be defined a sufficient radial distance from the fire location so that the influx (entrainment) specification does not affect the overall solution: mathematically the proper boundary conditions are defined at infinity. Further, the actual fuel vaporization rate is controlled by the heat radiated from the fire to the liquid pool, so that the evaporation rate boundary condition is both time-dependent and ill-posed in the sense that it depends on the solution for the overall fire structure (which itself depends on the boundary conditions applied). The entrainment boundary conditions are more easily specified in the case of a fire in a crosswind, for in this case, the mean velocity profile approaching the fire can be defined directly, so that although the crosswind fire problem is three-dimensional whereas the zero wind fire is axisymmetric, the former problem is more easily posed. However, the problem of specifying the boundary condition at the fuel surface still remains: defining a constant vaporization rate, as was done in the parabolic computations reported herein, is at best a crude approximation.

Thus, although a parabolic pool fire model is a rough approximation to reality for the zero-wind case, the development of a more exact approach is itself problematical and involves a several orders-of-magnitude greater effort, both in development and in solution time. The approximations involved in the parabolic formulation improve progressively as height above ground increases, so that if what is desired is fire structure and transport data

three or more pool radii above the fire surface, the parabolic model should suffice. This will be demonstrated, at least in part, by the comparisons of model predictions with experimental data to be described in the next section of this report.

3. COMPARISON OF MODEL RESULTS WITH POOL FIRE DATA

On the basis of the centerline temperature comparisons shown in Section 2 of this report, the Alpinieri eddy viscosity approach, with coefficients of 0.07/0.005, changing at one radius above the liquid pool, using the unmixedness model with the factor $f = 0.75$, and the thin gas radiation approximation with an emissivity of 0.50, was selected for detailed comparison with the experimental data obtained from the NASA-White Sands test program. It is clear from the comparisons shown in Section 2 that, because of the close coupling of each of these parameters in the overall pool fire model, large variations in predicted results can be obtained with variations in these parameters. Thus the set of parameters selected for the comparisons to follow do not represent an "optimum," but rather represent physically reasonable values which provide a reasonably good prediction of the centerline temperature profile observed during the experimental program.

3.1 RADIAL TEMPERATURE PROFILE PREDICTIONS

Model predictions of the radial temperature profiles for each of the vertical stations at which temperature data were obtained are shown in comparison with the data in Figs. 13-17. At low altitudes in the fire, peak temperatures are strongly overpredicted by the model, as evidenced by the 1.43 meter results shown in Fig. 13, and the 2.87 meter results shown in Fig. 14. However, in both of these cases the bimodal character exhibited by the experimental data is well represented, with the spatial location (if not the magnitude) of the temperature peak agreeing reasonably well with that measured in the experiments. At a height of 5.73 meters, the peak temperature is still overpredicted, and the predicted bimodal structure is more pronounced than that shown by the experimental data, as can be seen from Fig. 15. At this vertical location the predicted temperature profile is also considerably wider than the data indicate. This anomaly was observed in all calculations of the 15 meter (50 foot) diameter fire that were carried out: although the temperature profile width is in general well represented for measurement stations other than that at 5.73 meters, it is not well represented *at* 5.73 meters. One possible cause of this anomaly could be an offset in the experimental centerline at this point, but note that the data from both of the

43

15 meter (50 foot) fire tests overlay reasonably well at this point. Another possible cause may be the accumulated effects of the two rows of sample elements located below this height, but a mechanism that would produce the observed effects has not been identified.

It should be recalled from the discussion in Section 2.8 that each of the profiles so far described is in the region in which the approximations inherent in the parabolic formulation can, on the basis of computed stream function patterns alone, be expected to be the least applicable. In fact, it was observed in Section 2.8, on the basis of preliminary computations in which higher predicted temperatures and thus larger effects of buoyancy than in the model currently being discussed were evident, that from the stream function pattern it did not appear that reasonable results would be achievable with a parabolic model at distances less than two or three pool radii from the liquid surface. However, the results shown in Figs. 16 and 17 indicate that very good radial profile results are, in fact, achieved for h = 11.48 and 21.43 meters, or h/r_p = 1.54 and 2.86, respectively.

3.2 SPECIES PREDICTIONS AND COMPARISON WITH EXPERIMENT

A variety of data, encompassing both radial and axial profiles, is available for the chemical species observed in the 15 meter (50 foot) diameter fire tests. The data include measurements of O_2, N_2, CO, CO_2, soot and unburned fuel. It should, however, be noted at the outset of these comparisons that the chemistry model used in the pool fire code was, as described in Section 2.8, designed primarily to obtain reasonable temperature predictions, and not to predict in detail the species mass fraction distributions within the fire plume. Indeed, as will be seen, the experimental data indicate a considerably slower overall rate of reaction than that predicted by the quasi-equilibrium model utilized in the pool fire analysis. Nevertheless, a comparison of predicted and measured species distributions is of some interest.

Detailed radial profile data are available for the 5.73 meter height, and the measured and predicted O_2 and N_2 profiles at this height are compared in Figs. 18 and 19. It will be recalled from the discussion of the temperature comparisons that at this height the thermal extent of the fire was overpredicted, and it can be seen from Figs. 18 and 19 that at this height the width
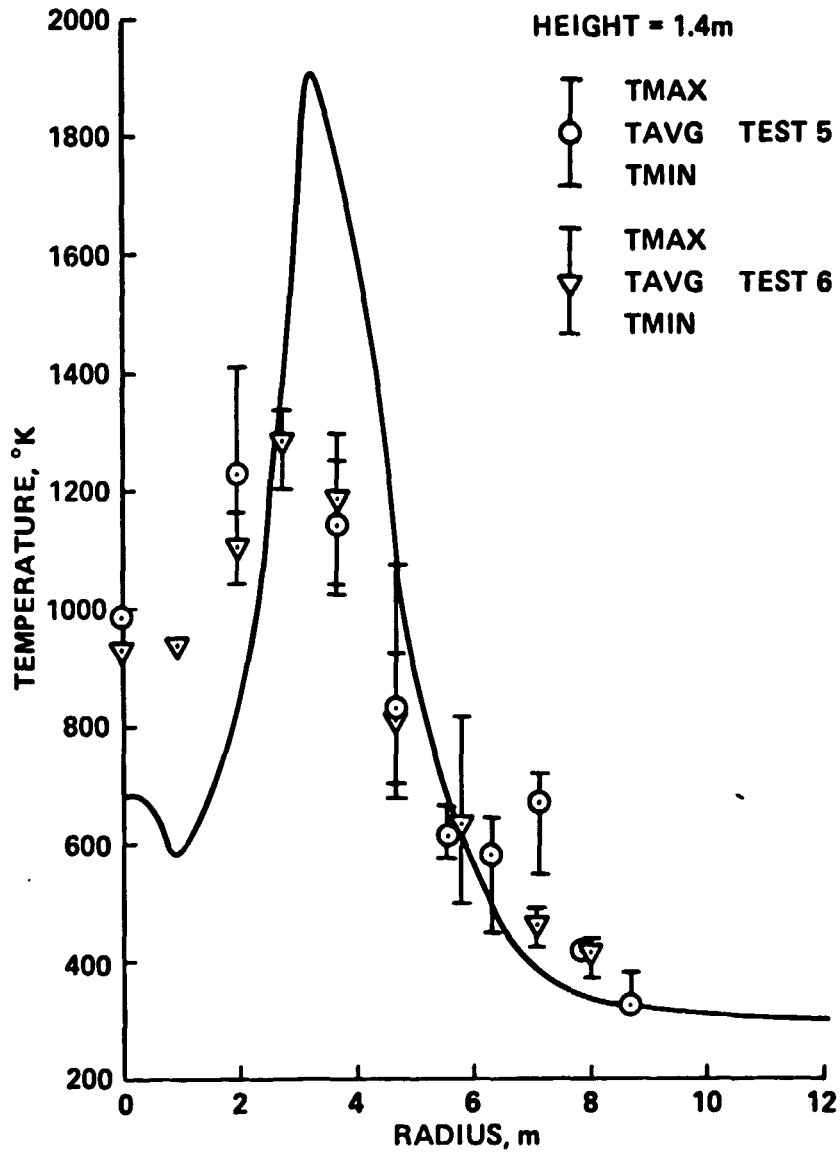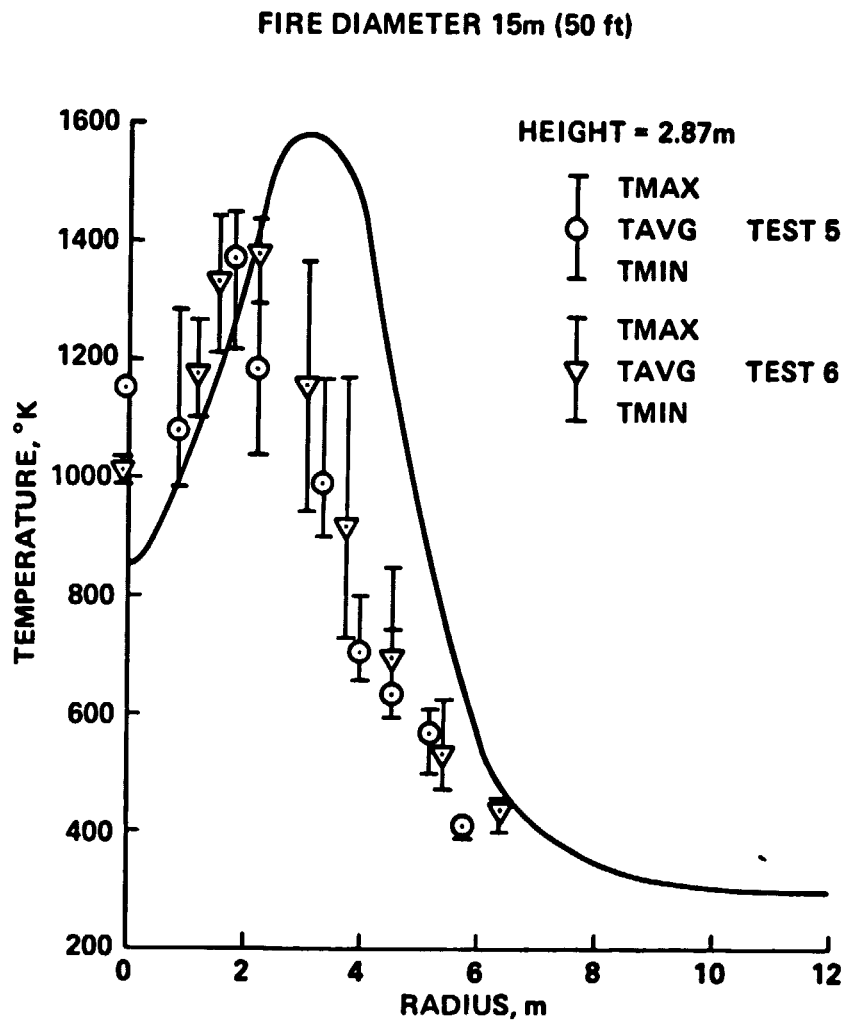
FIRE DIAMETER 15m (50 ft)

FIGURE 13. Radial Temperature Profiles at 1.4 Meters
15 M (50 ft) Diameter Pool Fire

FIGURE 14. Radial Temperature Profiles at 2.8 Meters
15 M (50 ft) Diameter Pool Fire.
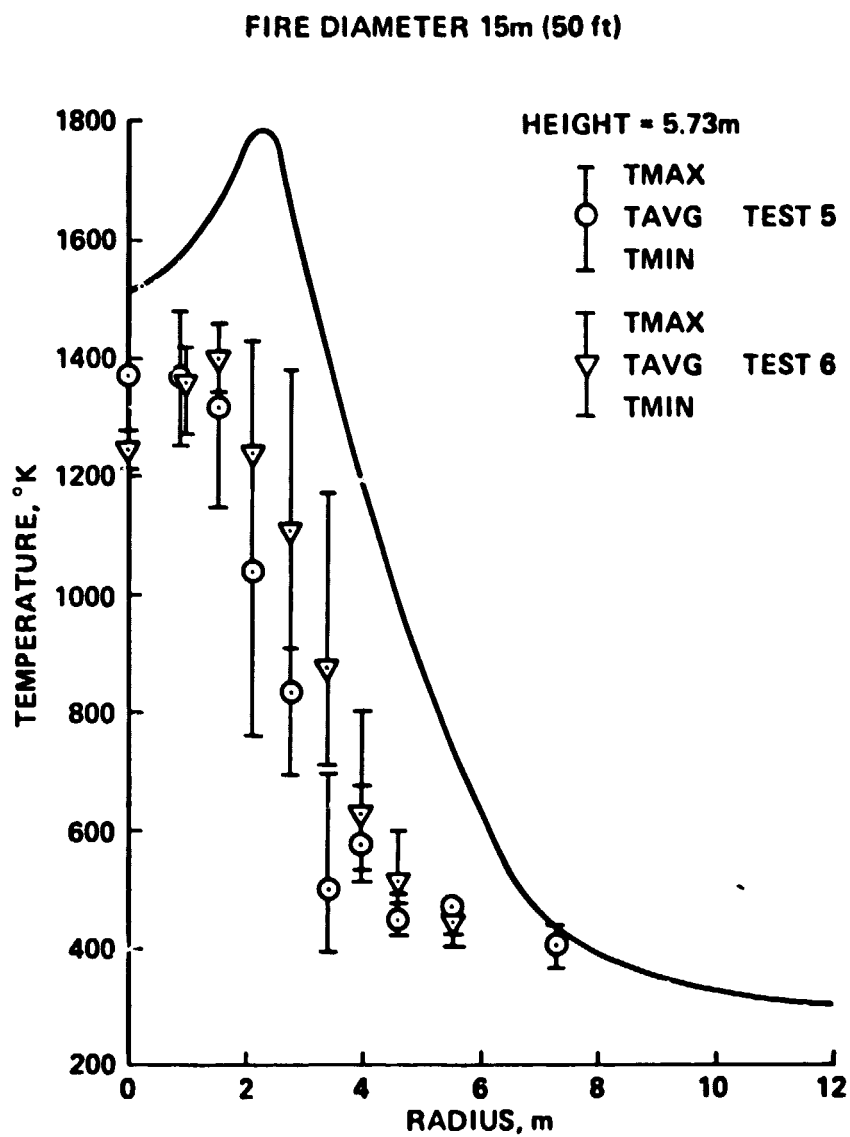
FIRE DIAMETER 15m (50 ft)

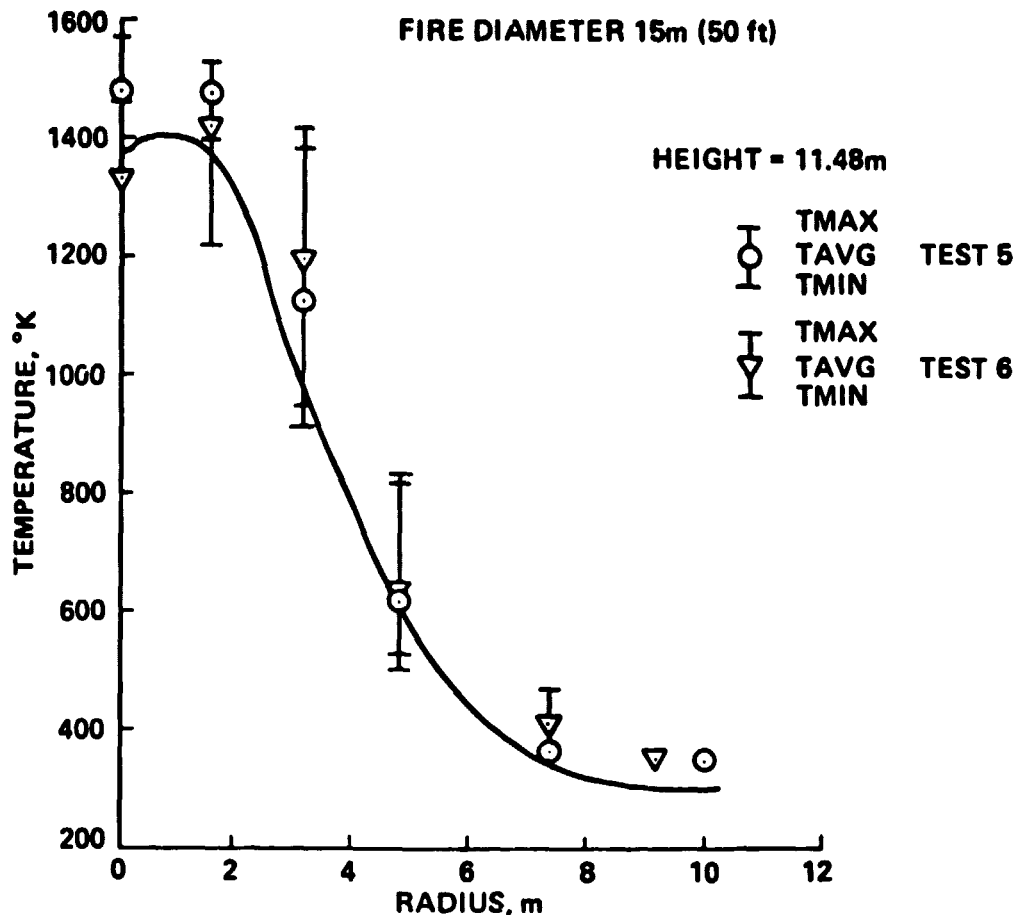FIGURE 15.   Radial Temperature Profiles at 5.7 M
15 M (50 ft) Diameter Pool Fire

FIGURE 16.   Radial Temperature Profiles at 11.5 M
15 M (50 ft) Diameter Pool Fire

of the fire plume as evidenced by both the O_2 and N_2 concentrations is over-predict d as well. Note that in the computations the turbulent Prandtl and Lewis numbers were both assumed to be unity, so that the element mass fraction and total enthalpy prcfile widths will be equivalent ard identical to the velocity profile width as well. As was the case for the temperature profile, although the magnitude of these concentration profiles is not well predicted, the general shape of the profiles is accurate (disregarding the possibly anomalous centerline nitrogen mass fraction value shown on Fig. 19).

Centerline values of the fuel mass fraction are of considerable interest in assessing the overall behavior of the model, and in interpreting the experimental results. A comparison of computed centerline fuel concentration with experimental data for this parameter is shown on Fig. 20. The data

FIRE DIAMETER 15m (50 ft)

HEIGHT = 21.43m

TMAX
TAVG   TEST 5
TMIN

TMAX
TAVG   TEST 6
TMIN
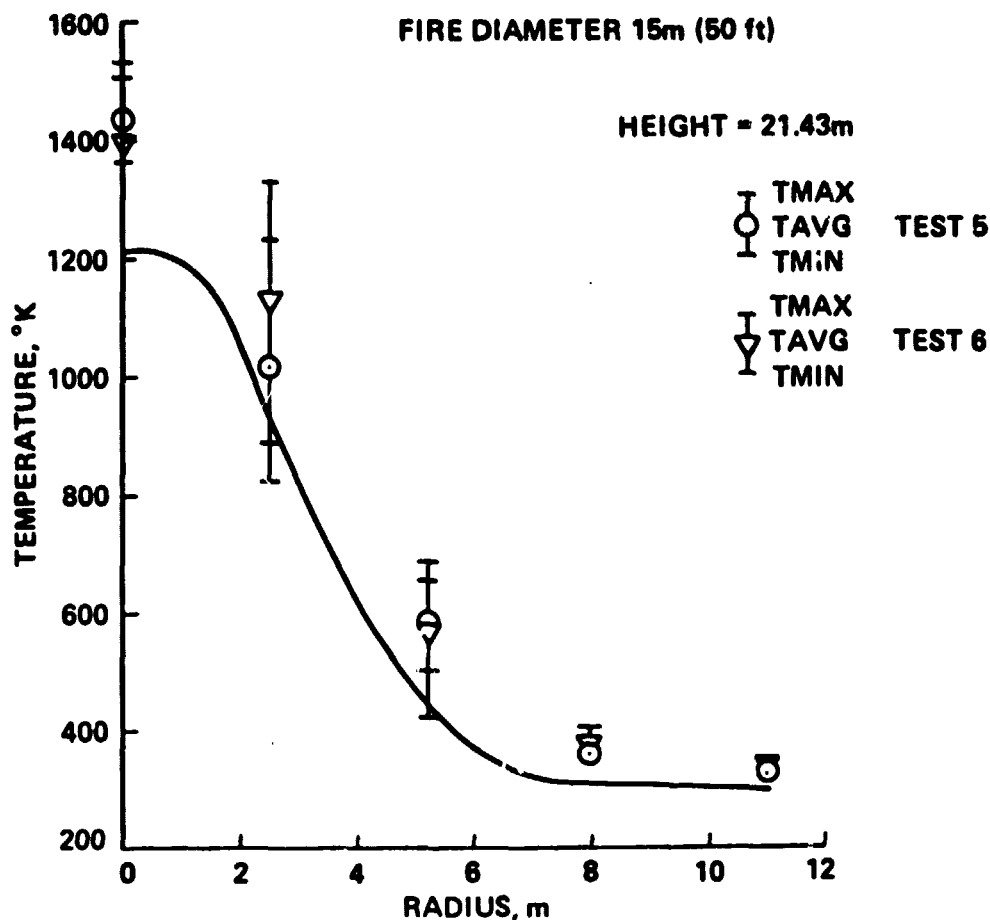
FIGURE 17.   Radial Temperature Profiles At 2.14 M
15 M (50 ft) Diameter Pool Fire

indicate persistence of fuel along the centerline until about two pool radii
above the pool surface, and this long persistence of fuel is not predicted
by the computations. Note again, from Fig. 20, the improvement in the predic-
tion relative to the experimental data that is generated by the use of the
unmixedness model. Although the unmixedness model used in these computations
is by no means a rigorous treatment of the phenomenon, but is rather an
order-of-magnitude estimate, the fact that even with the incorpration of
unmixedness the computed fuel concentration is, below about 11 meters, consider-
ably lower than that measured, provides evidence that the fuel consumption rate
is much slower than would be predicted by equilibrium chemistry.

It will be recalled that for temperatures above 750°K, a major branch
of the quasi-complete-equilibrium chemistry model involves the production of
CO and soot, at fuel-rich equivalence ratios. This branch of the model is
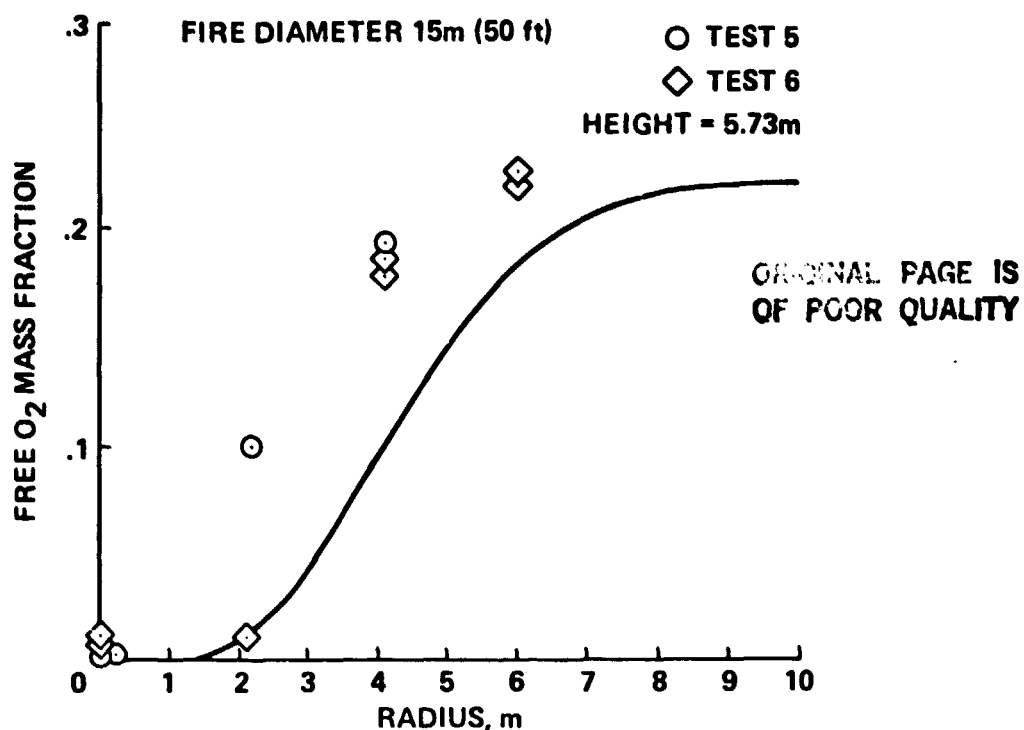
FIGURE 18. Comparison of Predicted and Measured O_2 Radial
Profiles, 15 M (50 ft) Diameter Fire
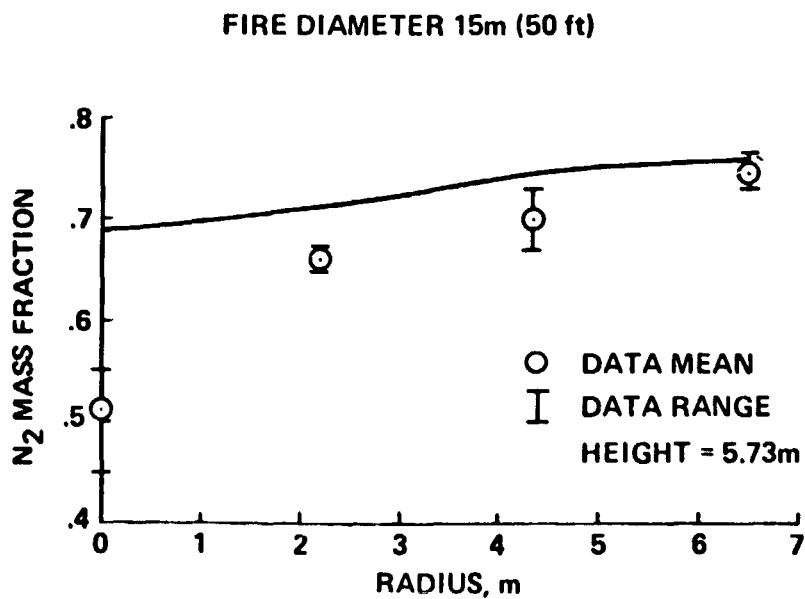
FIGURE 19. Comparison of Predicted and Measured N_2 Radial
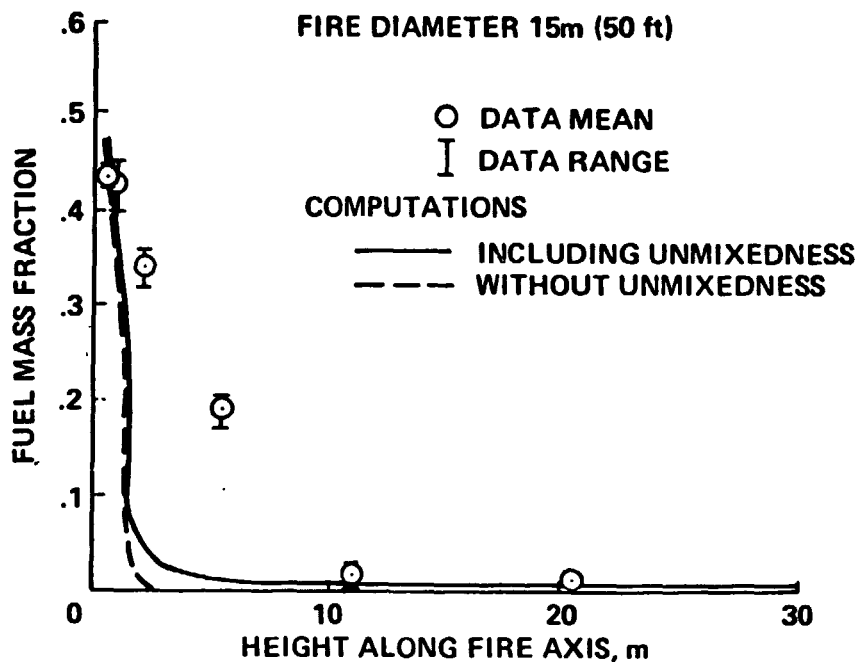Profiles, 15 M (50 ft) Diameter Fire

FIGURE 20. Comparison of Predicted and Measured Centerline
Fuel Concentration, 15 M (50 ft) Diameter Fire.

reached relatively early in the fire development, as evidenced by the CO and
soot mass fraction profiles shown in Figs. 21 and 22. As the local equivalence
ratio drops, the CO_2-H_2 branch is activated, and as the equivalence ratio
becomes less than unity, the products of combustion become CO_2 and H_2O. The
advent of these branches of the model is shown on Fig. 23. Both the early
CO and soot mass fractions are strongly overpredicted, which is consistent
with the rapid disappearance of fuel shown in Fig. 20. Taken together, these
three comparisons provide a further indication that the fuel consumption in
the fire is highly nonequilibrium process, as well as one which is strongly
affected by turbulence-chemistry interaction or unmixedness phenomena.

At the conclusion of this comparison, it should be reiterated that the
chemistry model used in the fire model is intended to provide reasonable temper-
ature estimates but not necessarily to predict the observed species distribu-
tions. Indeed, the measured species data obtained in the 15 meter (50 foot)
fire experiments strongly indicate the nonequilibrium nature of the chemical
processes occurring within the fire. A quasi-complete equilibrium formulation
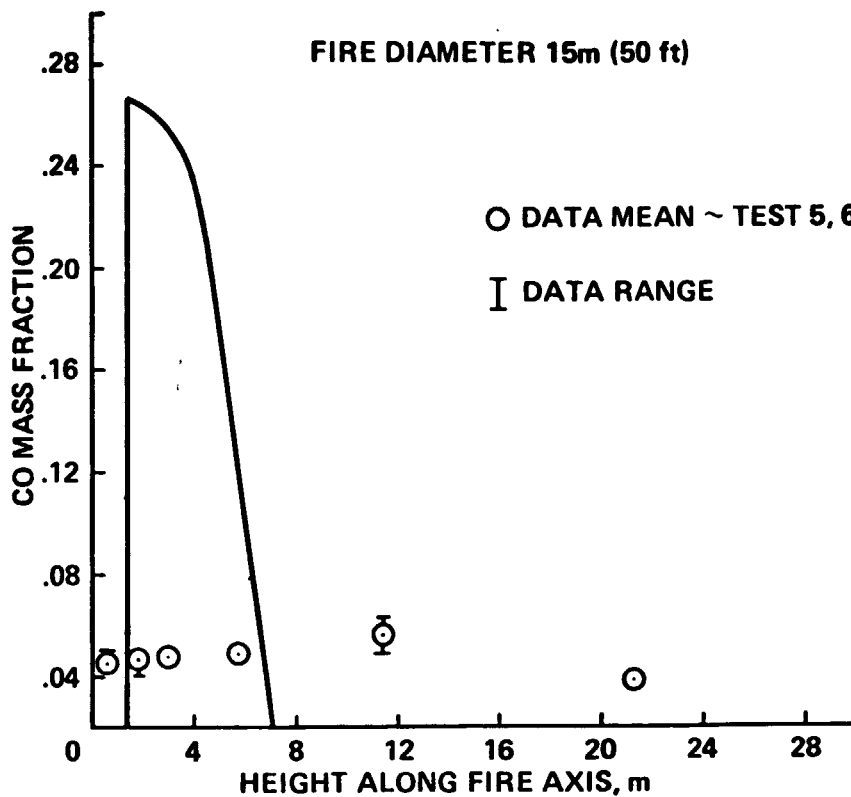cannot be expected to adequately model the processes that are observed.

FIGURE 21. Comparison of Predicted and Measured Centerline
CO Concentration, 15 M Fire.

3.3 RESULTS FOR OTHER FIRE SIZES AND FIRE SCALING

In addition to the computations of the 15 meter (50 ft) and fire, computa-
tions were also carried out for a 7.6 meter (25 foot) and a 3:8 meter (12.5 ft)
diameter pool fire. In general, the results obtained for the smaller sizes
were similar to those already discussed for the 15 meter (50 ft) diameter
fire, and these results are summarized in the form of isotherm and iso-soot-
concentration contour plots in Figs. 24-29. These figures show that the basic
features of each of the fires are quite similar, with a characteristically
bimodal temperature distribution being seen at the base of the fire, followed
by a high-temperature plume. Qualitatively, the isotherm distribution that is
computed using the parabolic model is also quite similar to that observed
experimentally, Fig. 30, although there are some quantitative differences.
In general, however, the computed results provide a good overall picture of
the thermal environment within the fire. Soot distribution profiles are shown
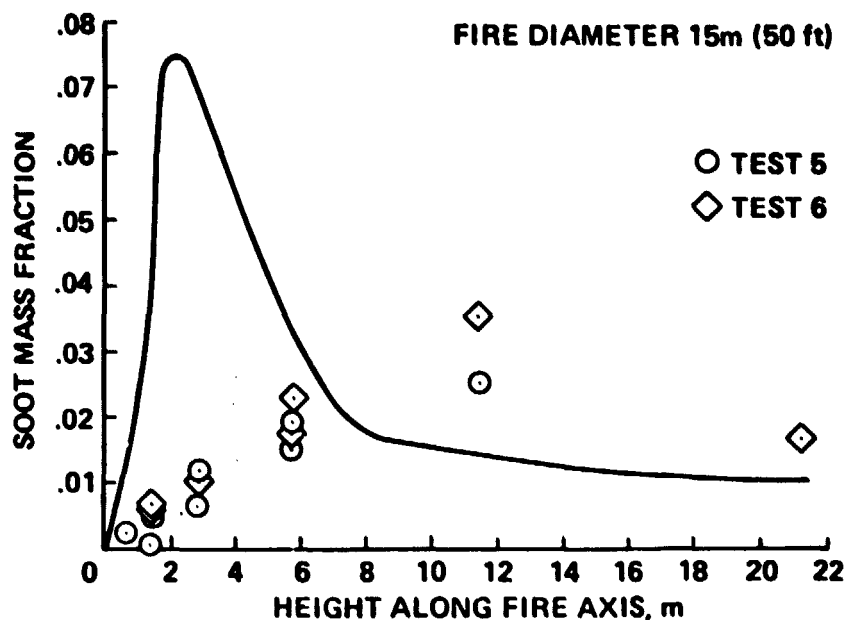in Figs. 25, 27, and 29; although the comparisons with experimental data

FIGURE 22.   Comparison of Predicted and Measured Soot Concentrations
Along Fire Centerline, 15 M (50 ft) Diameter Fire

described in the previous section indicate that the model overpredicts the initial soot concentration, the comparison of results for the different fire sizes indicates that the soot concentration profiles for each of the fire sizes are also qualitatively similar. Fig. 31 is an overlay of the computed isotherms for the 15 meter (50 ft) diameter fire on a drawing made from a photograph of one of the fire tests; since the detailed comparisons indicate that the computations are in general agreement with experimental results for this fire size, this overlay provides an interesting depiction of the flame structure.

For many turbulent flows, geometric scaling holds provided the Reynolds number is large enough; i.e., for nozzles twice the diameter, the length to a given level of mixing is twice as long. Rigorously, this scaling applies only when the source terms in the governing equations are either zero or negligibly small. This is not the case for these fire calculations, in which the buoyancy term provides a nonnegligible source term for the momentum equations. However, as Fig. 32 shows, the centerline temperature profiles for the 15 meter and 7.6 meter fires scale reasonably well, while results for the smallest fire size studied fall below those for the other two sizes. Note that
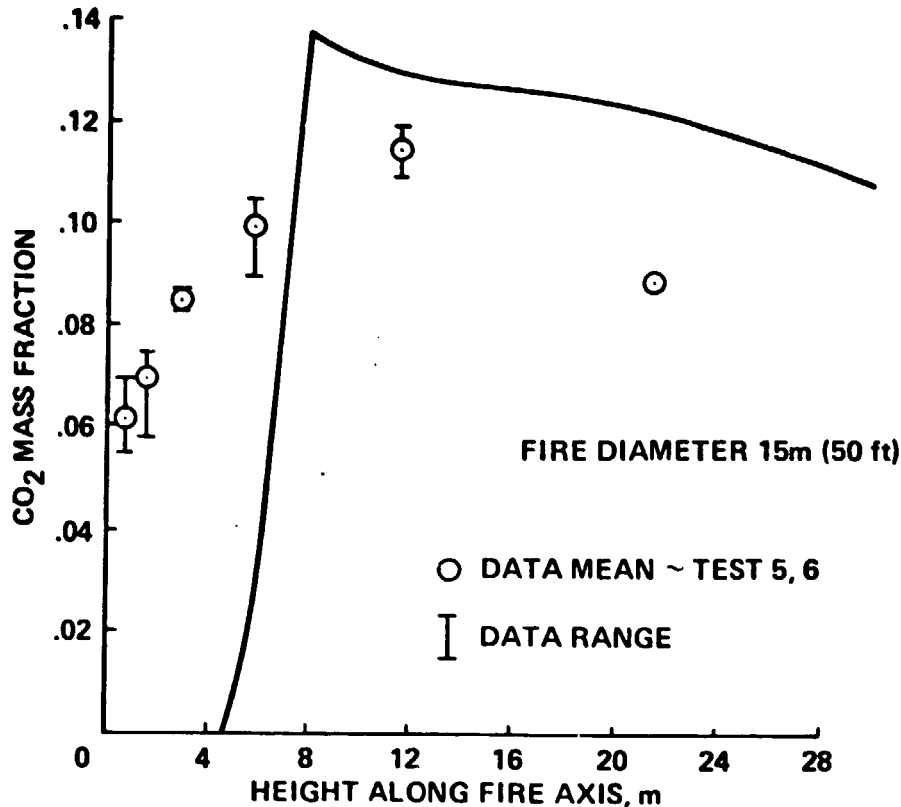
FIGURE 23. Comparison of Predicted and Measured Centerline
CO_2 Concentrations, 15 M Fire.

the axial location of the peak centerline temperature scales almost exactly,
although it should be recalled that in the region of peak centerline temperature
the assumptions basic to the use of a parabolic fire plume model are not well
met.

Centerline velocity profiles are also of interest, both from the standpoint
of scaling and because the magnitudes of the velocities encountered in fire
plumes of this large scale often tend to be underestimated. Fig. 33 shows
centerline velocity results for the three fire sizes. Here it is evident that
geometric scaling does not apply, and that velocities of the order of 30 m/sec
can be encountered in large-scale fires. The data point indicates on Fig. 33
was obtained during the NASA/White Sands test program, for a 15 m (50 ft)
diameter fire, using an anemometer designed by A. D. Little, Inc. to function
under extreme ambient conditions existing within the fire. The predicted
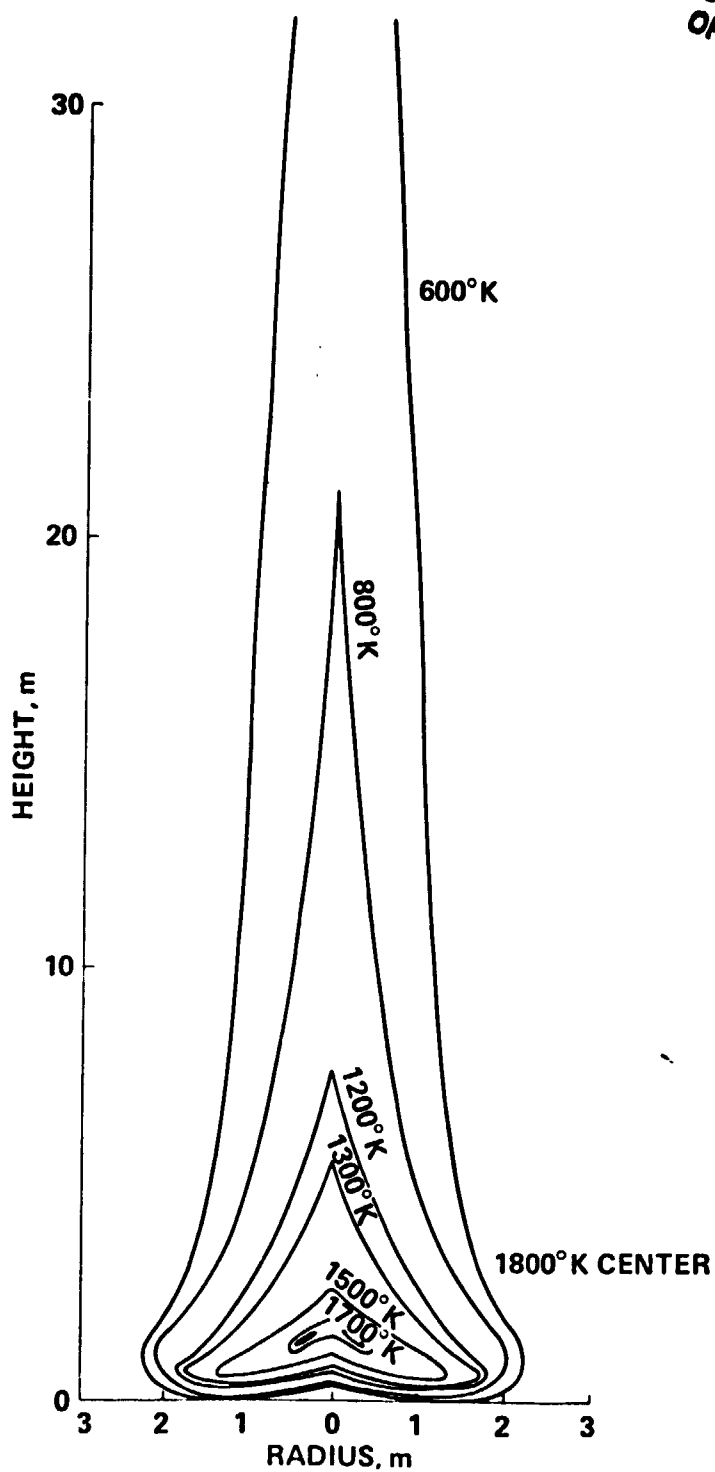centerline velocity for the 15 m (50 ft) fire is somewhat higher than this
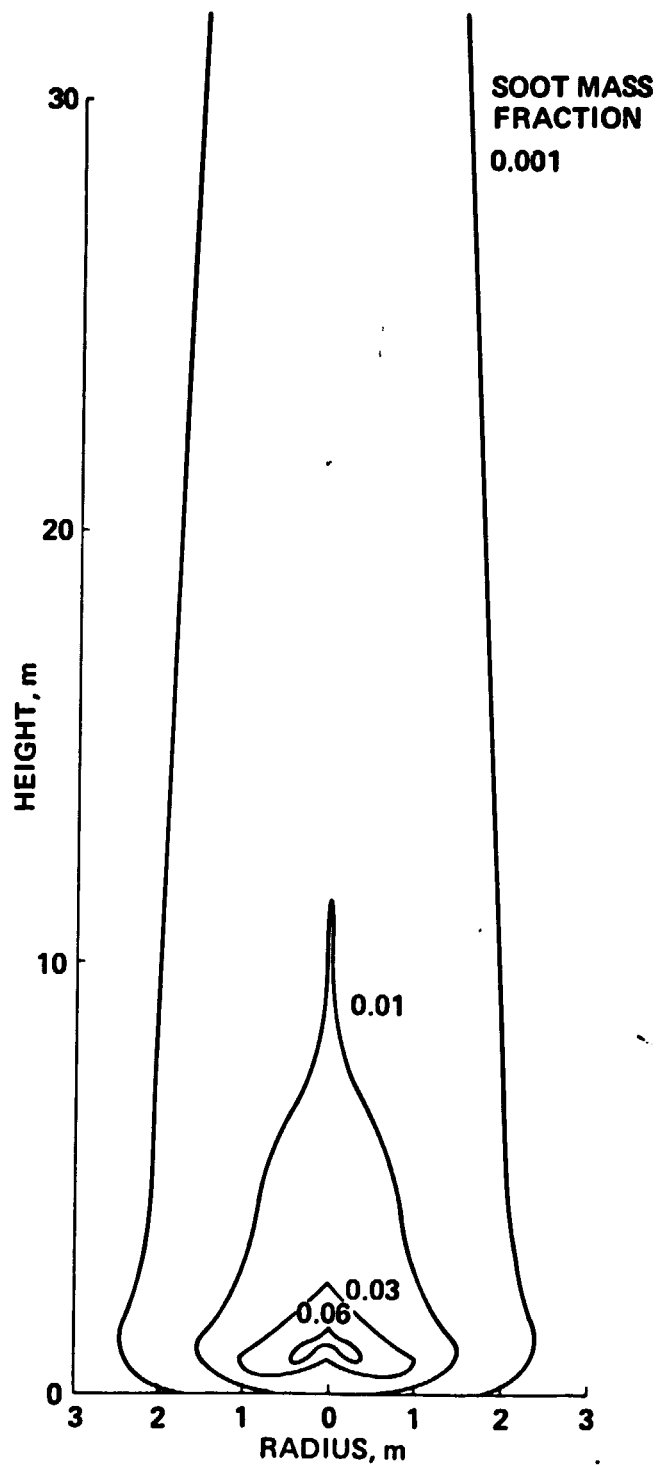
FIGURE 24.   Predicted Isotherm Contours, °K, For 3.8 M
(12.5 ft) Diameter Pool Fire

FIGURE 25. Predicted Soot Mass Fraction Contours,
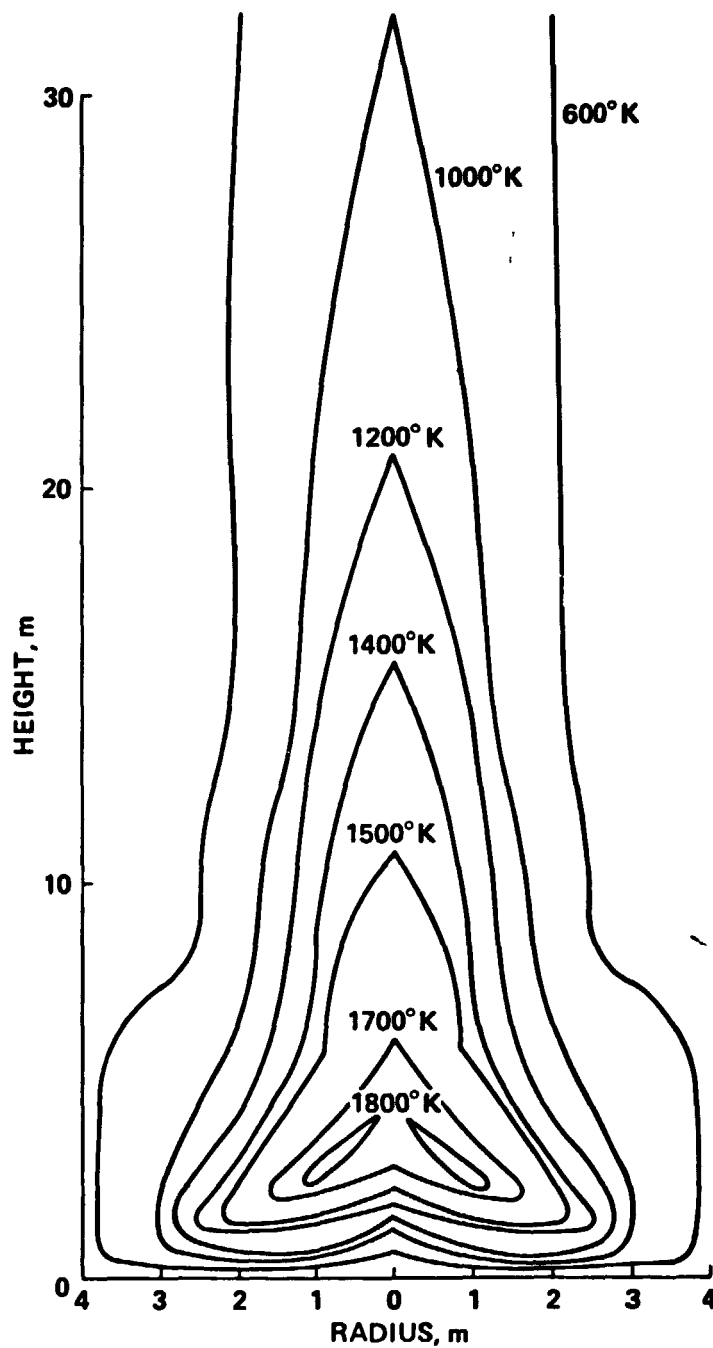3.8 M (12.5 ft) Diameter Pool Fire

FIGURE 26.   Predicted Isotherm Contours, °K, 7.6 M
(25 ft) Diameter Pool Fire
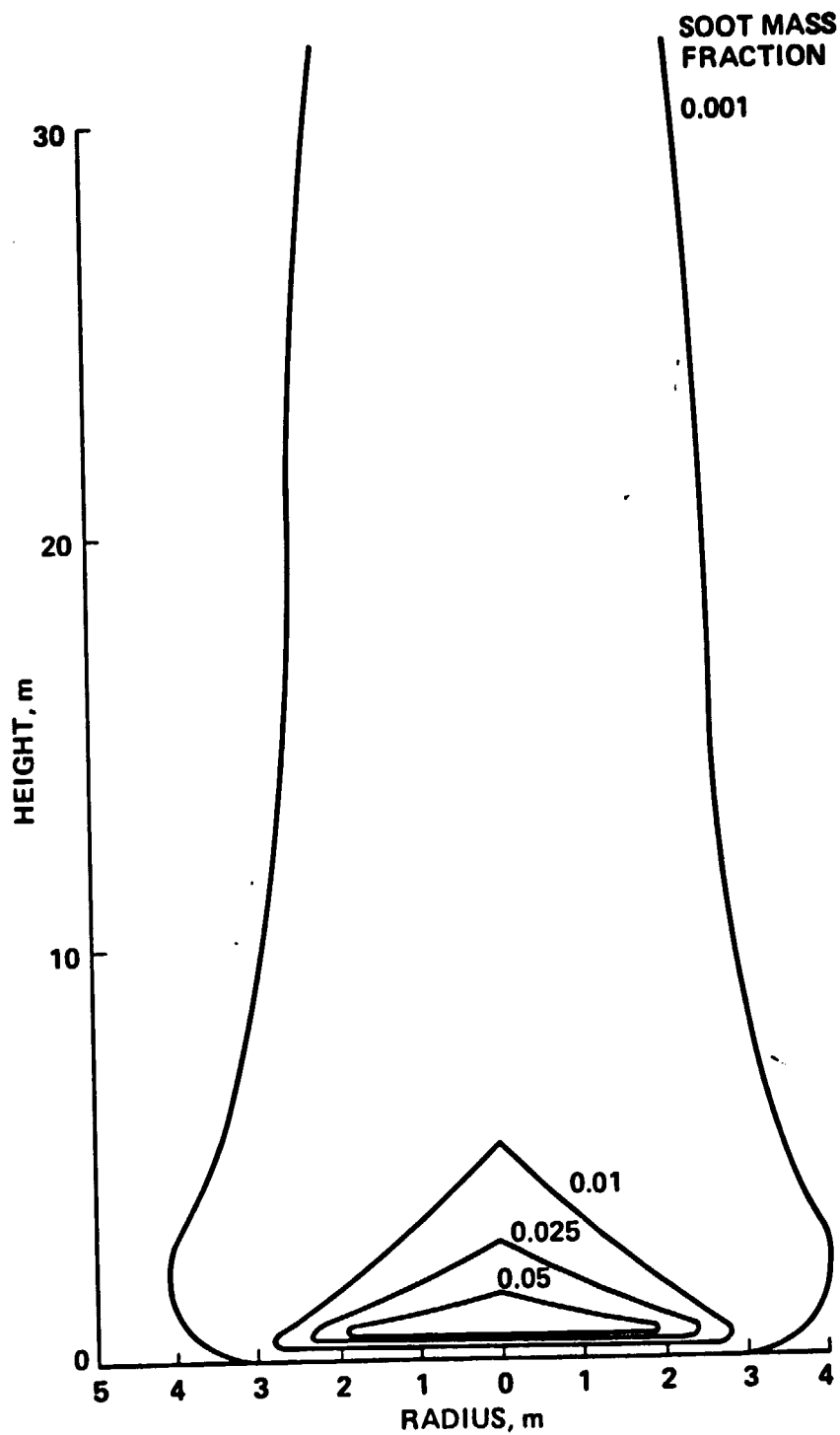
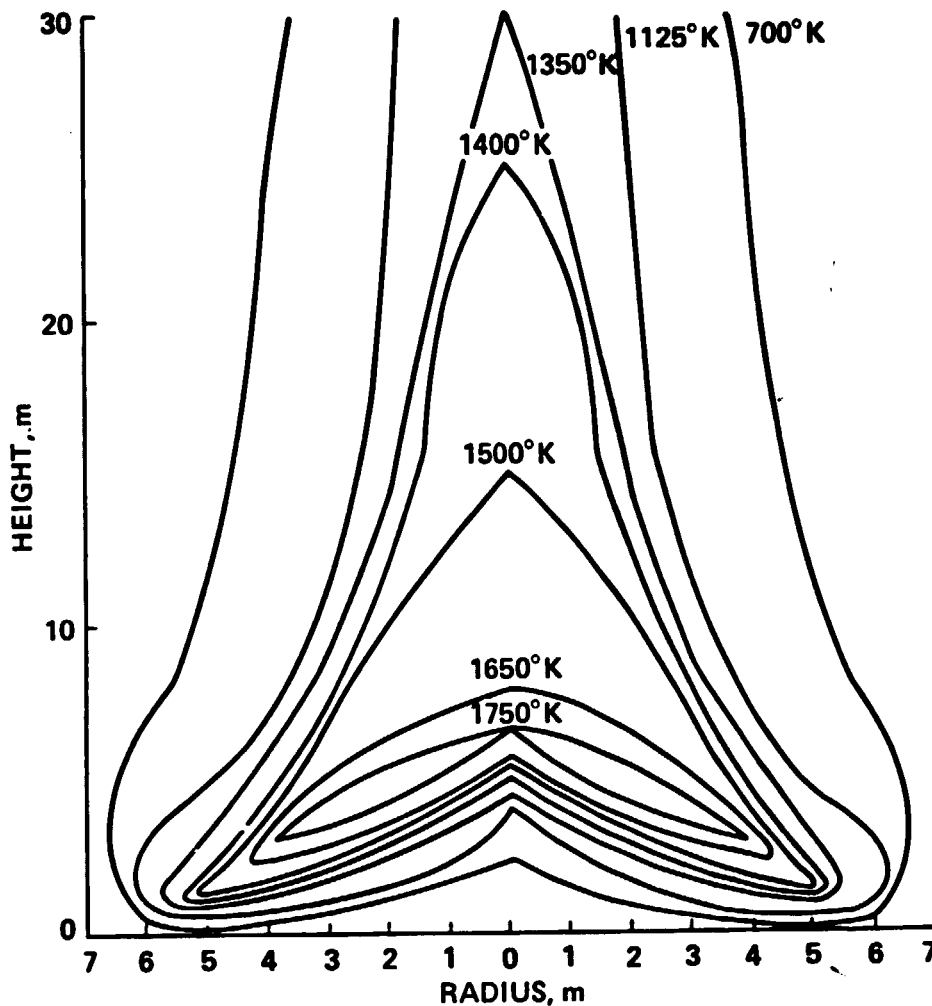FIGURE 27. Predicted Soot Mass Fraction Contours, 7.6 M
(25 ft) Diameter Pool Fire

FIGURE 28. Predicted Isotherm Contours, (°K), 15.2 M
(50 ft) Diameter Pool Fire

measurement indicates, but in the absence of an error estimate for the
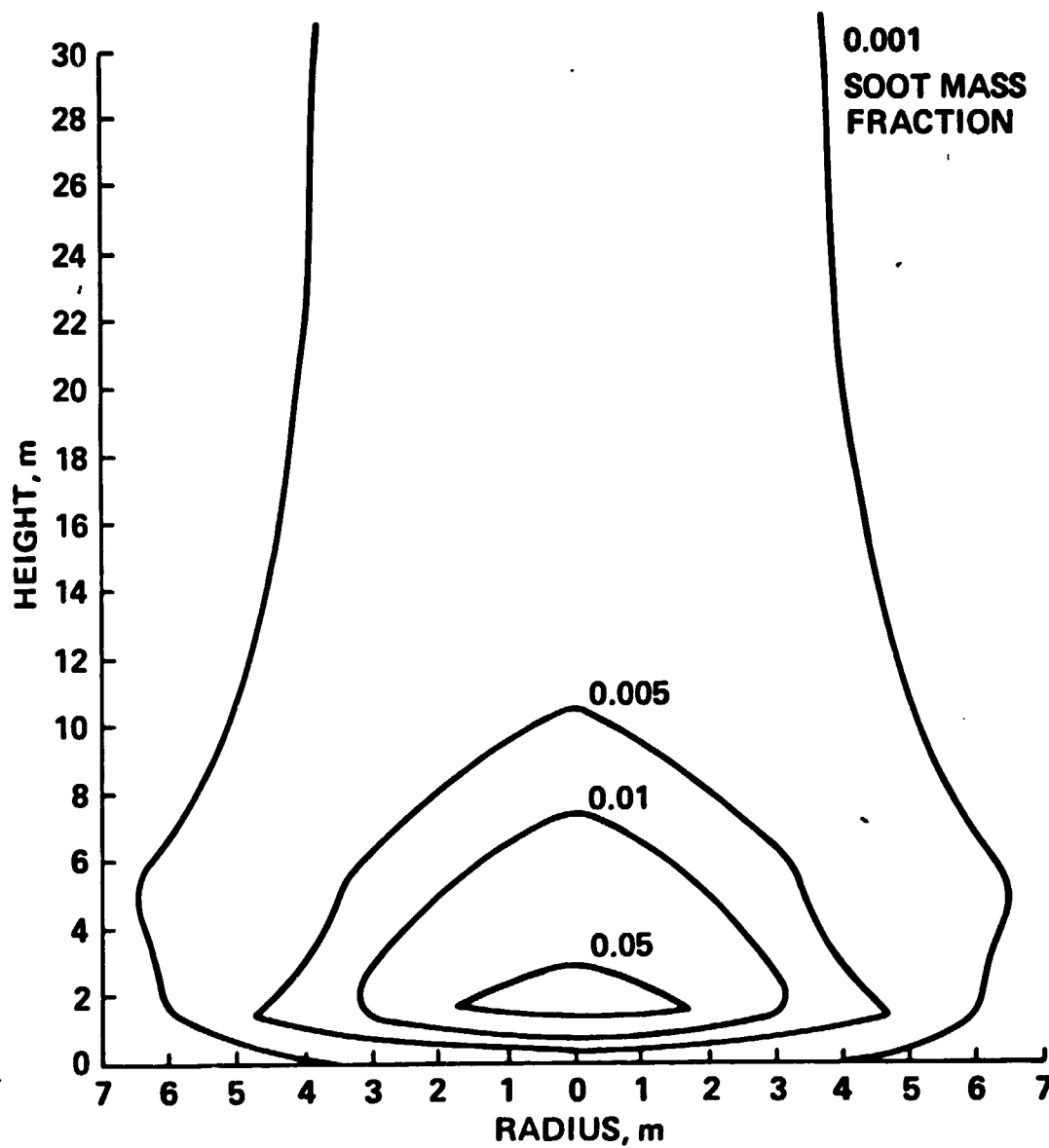instrument the level of agreement shown can be considered to be satisfactory.

FIGURE 29. Predicted Soot Mass Fraction Contours
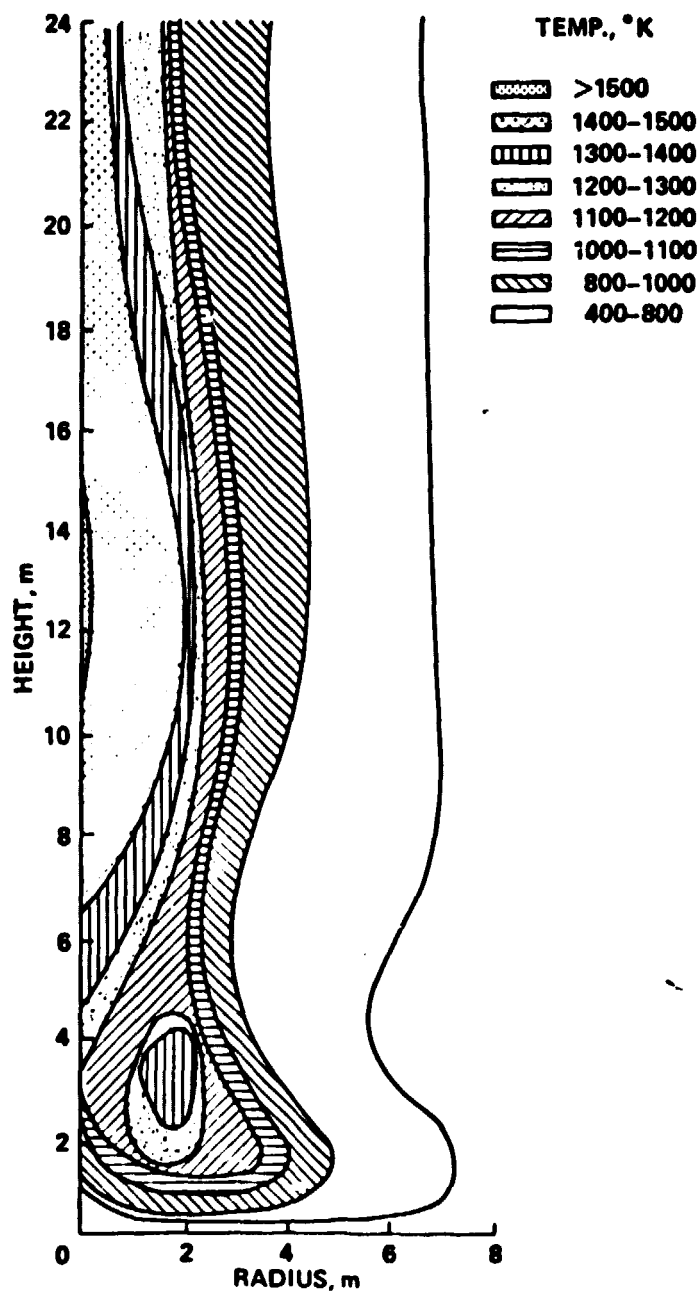15. 2 M (50 ft) Diameter Pool Fire

50 ft FIRE TEST 5

FIGURE 30. Isotherm Contours Obtained From Measurements
in 15.24 M (50 ft) Fire

TEMPERATURE, K
- 400
- 700
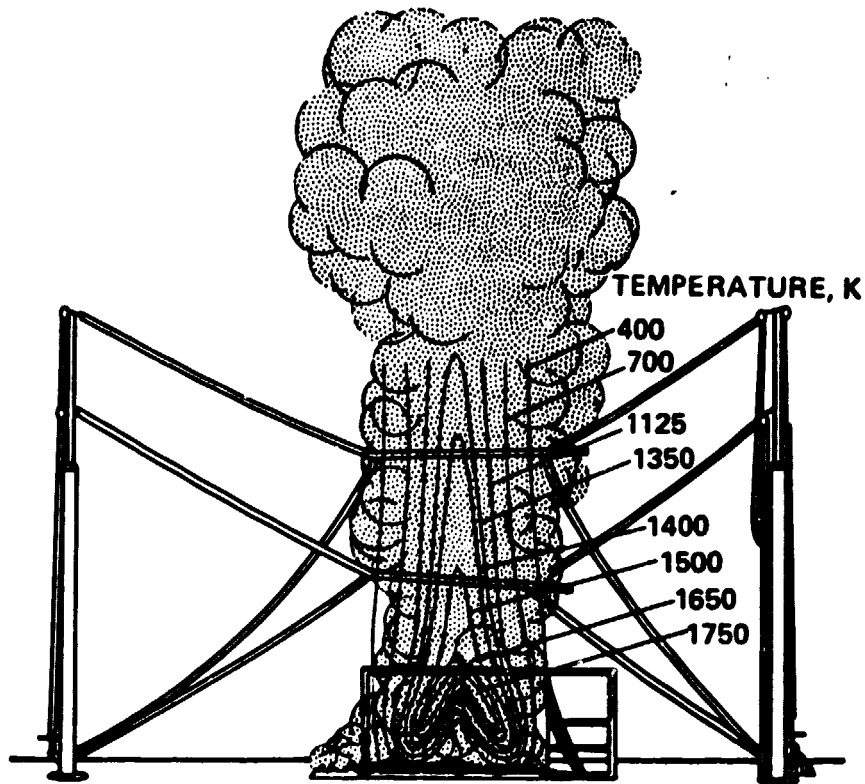- 1125
- 1350
- 1400
- 1500
- 1650
- 1750

FIGURE 31. Flame Structure Isotherm Overlay
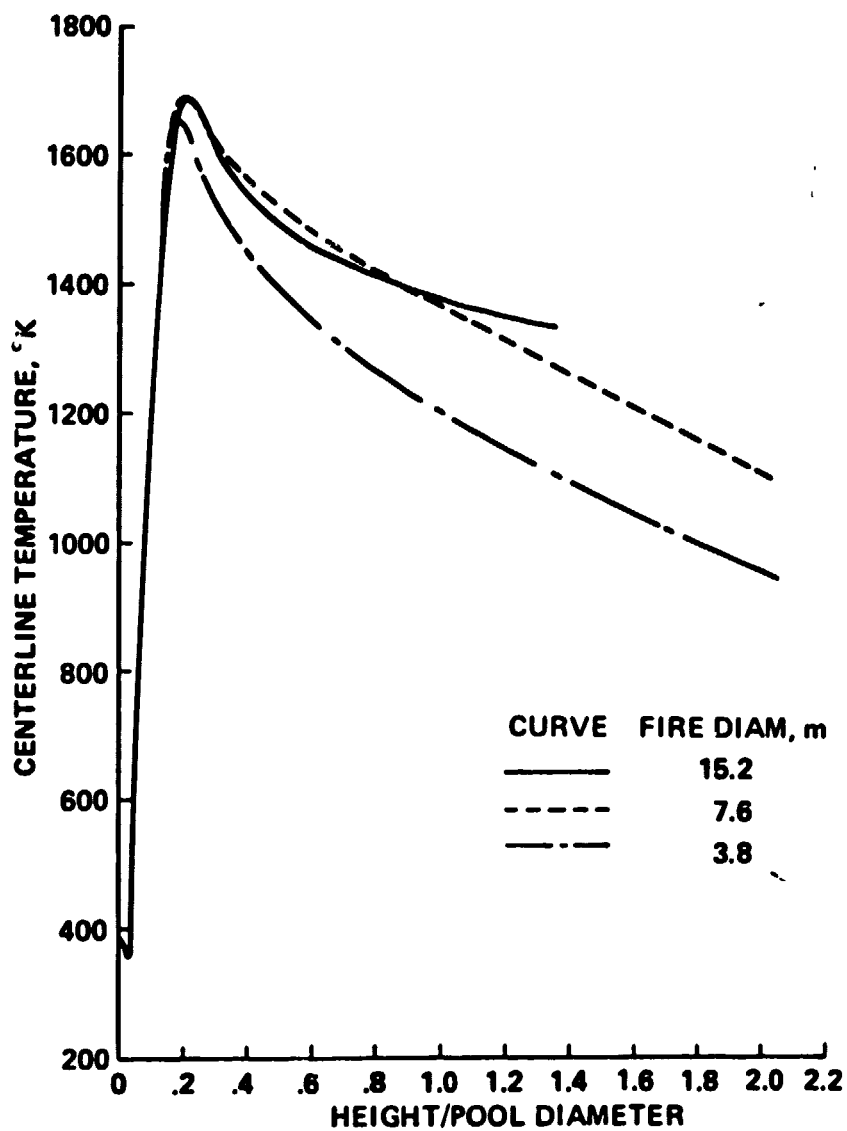
FIGURE 32. Centerline Temperature as a Function
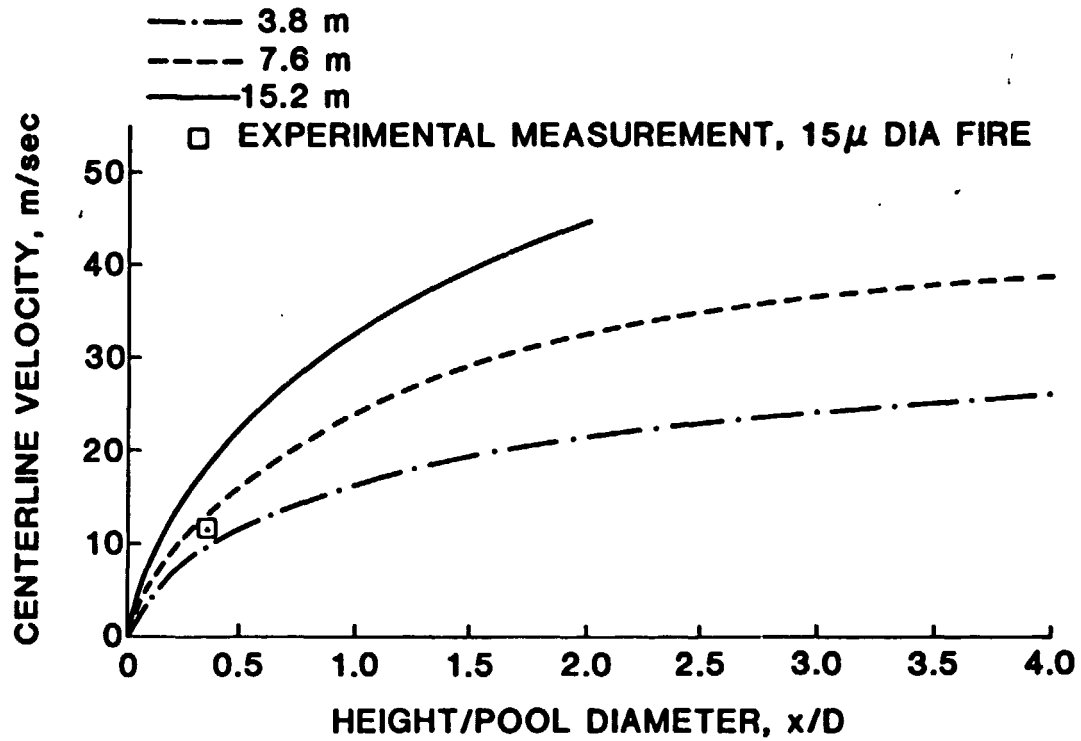of Scaled Distance From Pool

FIGURE 33.   Centerline Velocity as a Function of
Scaled Distance From Pool

4. PREDICTION OF FIBER FLUXES AND CONSUMPTION

The model described in the preceding section has been applied to the computation of carbon fiber transport and consumption within a fire plume. Similar initial conditions were used for all fire calculations: fuel vaporization rate of 8.5×10^{-3} cm/sec (0.20 in/min), particle release rate of 10 kg/min, distributed uniformly across the pool, a fuel vapor temperature of 400°K and an ambient temperature of 300°K. The particle characteristics for these computations were as follows:

Particle Class	r_p(cm)	ℓ_p(cm)	f_p(kg/min)	Remarks
1	3.5×10^{-4}	0.15	0.288	Single Fiber
2	3.5×10^{-4}	0.35	0.448	Single Fiber
3	3.5×10^{-4}	0.65	0.791	Single Fiber
4	3.5×10^{-4}	1.00	1.217	Single Fiber
5	3.5×10^{-4}	1.40	1.076	Single Fiber
6	3.5×10^{-4}	5.00	3.202	Single Fiber
7	3.5×10^{-4}	25.00	1.282	Open Fiber Cluster Long Single Fiber
8	5.12×10^{-3}	10.00	1.694	Large Fiber Cluster

4.1 FIBER CONSUMPTION PREDICTIONS

Fiber consumption rates were obtained as part of the work described in Ref. 4; although this parameter was not computed in more recent work, a comparison of the fire structure results presented herein with those presented in Ref. 4 indicates that the modifications made to the chemistry model in this work would not materially affect the fiber consumption results. In view of the thermal nonequilibrium results reported in Section 2.7, the thermal equilibrium assumption was retained for these calculations. Results, expressed as percent of total fibers consumed, are shown for the single fibers in Fig. 34: single fiber results are shown because these fibers are much more readily characterized in terms of geometric parameters (length, diameter, effective surface area, volume) than are the fiber clusters and clumps. These results show that the bulk of the fiber consumption occurs in the lower regions
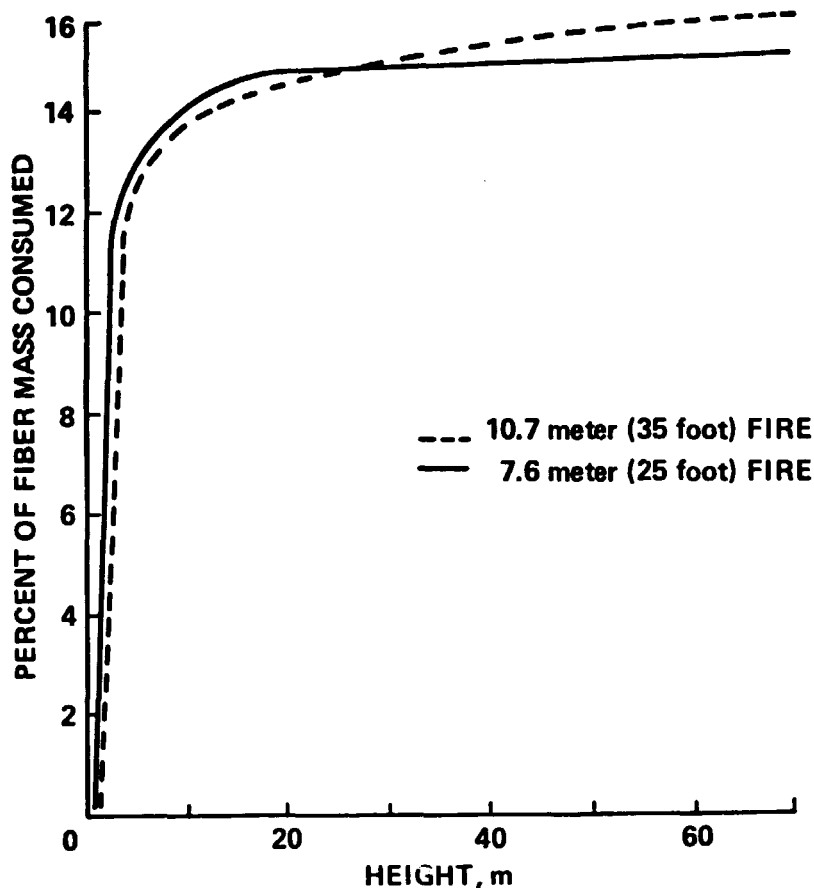
FIGURE 34. Fiber Consumption (Single Fibers) Computed
For Two Fire Sizes

of the fire. For the larger fire, the initial consumption at a given value
of height above the liquid fuel pool is lower than for the smaller fire since
the height at which the peak temperature occurs increases with pool diameter.
It is also evident that the total fiber consumption increases somewhat with
fire size, and that in both cases fiber consumption has ceased by the 60 meter
(200 ft) height in the fire.

4.2 FIBER FLUX PREDICTIONS

Fiber flux results for the single fibers are presented for three fire
sizes in Figs. 35-37. These results are presented as local fiber fluxes
(kg/m^2-sec) normalized with initial fiber flux: since the burning rate for
all single fibers is the same, because of the assumption that the surface

area of the ends of a cylindrical fiber can be neglected in the consumption calculation, and it has been assumed in these computations that all single fibers have the same turbulent diffusivity, these normalized curves can be used to relate the flux of any class of single fibers to its initial flux. The initial fiber flow rates used to generate these computational results have been tabulated at the beginning of this section.

In all cases, because of the tendency of the fire to "neck down," the large majority of fibers are observed, even at the 61 meter (200 foot) height, to be in a region within one pool radius of the centerline. In addition, this "necking down" tendency, as shown in Section 2.5.1, leads to high-altitude (~ 100 ft or greater) fiber concentration profiles that are essentially independent of the initial location of the fibers within the fuel pool at h = 0; therefore, the results shown in Figs. 35-37 can be used to estimate fiber fluxes for any arbitrary (but axisymmetric) initial fiber distribution.
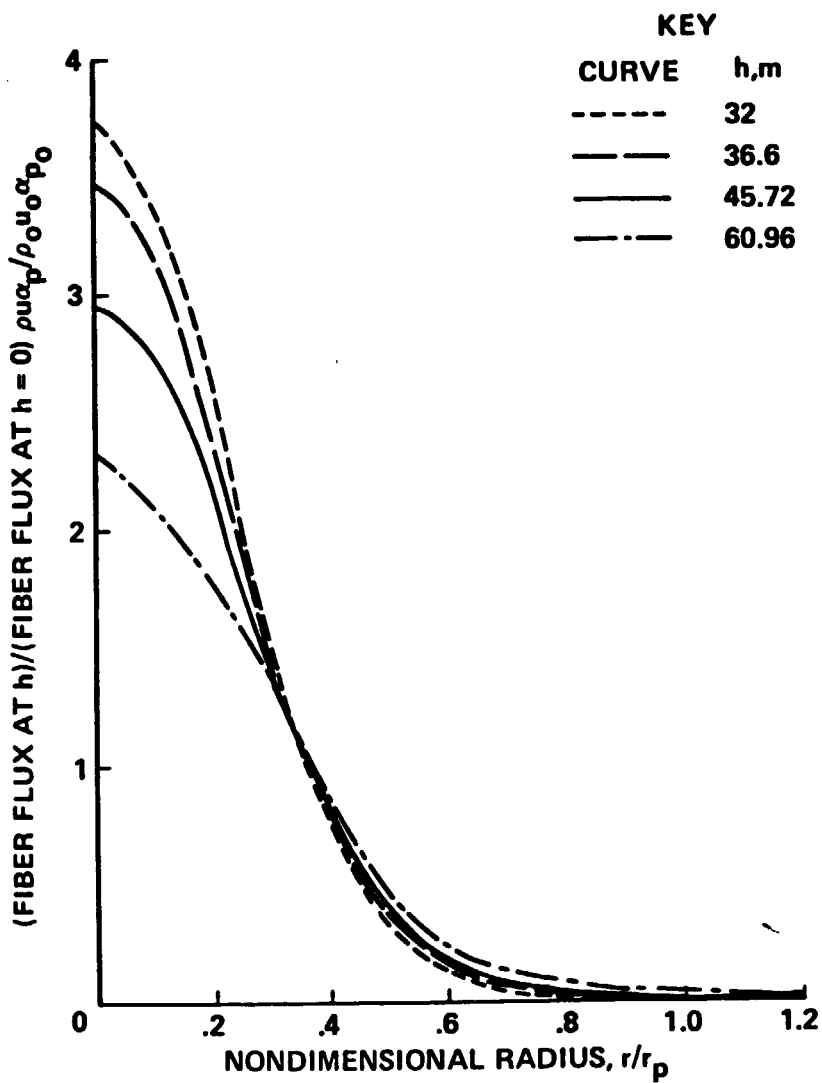
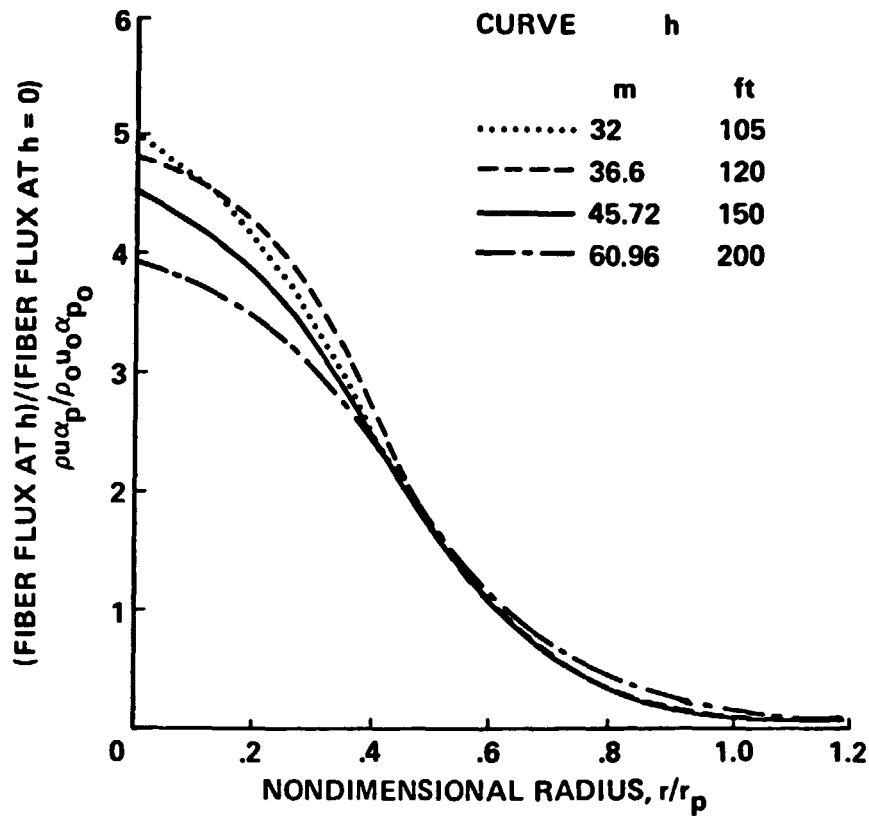FIGURE 35. Normalized Fiber Flux Profiles as a Function of Height, 3.81 M (12.5 foot) Diameter Fire

FIGURE 36. Normalized Fiber Flux Profiles as a Function of Height, 7.5 M (25 foot) Diameter Fire
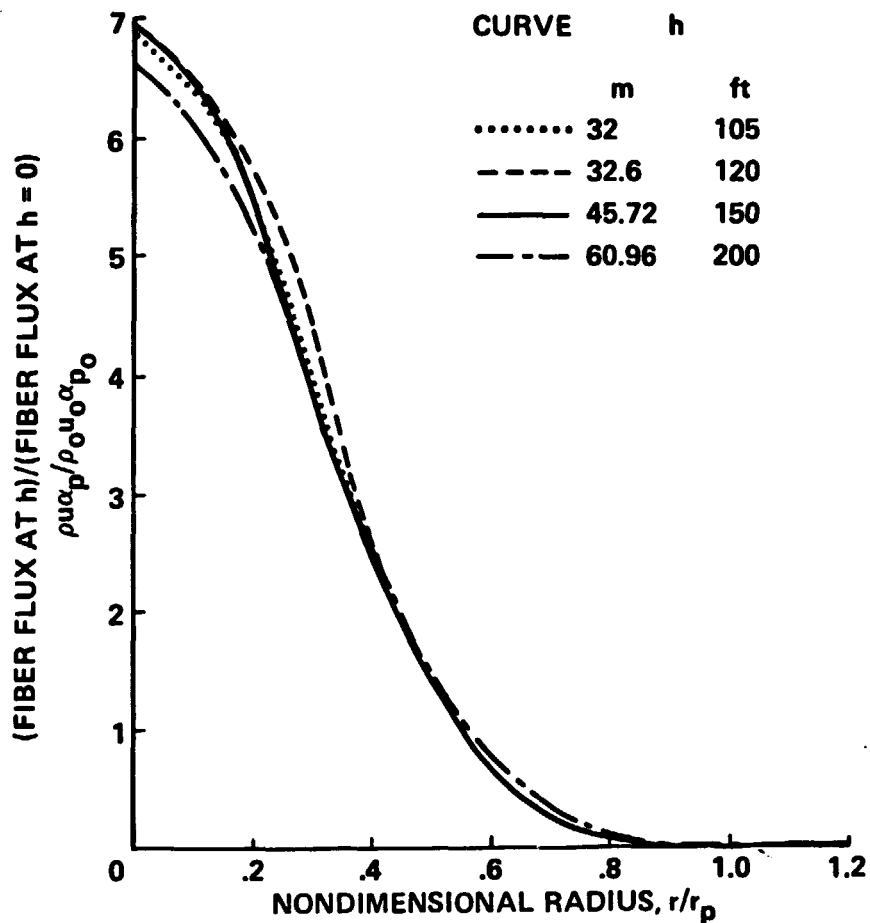
FIGURE 37. Normalized Fiber Flux Profiles as a Function
of Height, 15 M (50 foot) Diameter Fire

5. CONCLUSIONS

The result of the work outlined in this report has been the development of a model of pool fire phenomena which, although approximate, is capable of providing considerable detail of the structure of a pool fire in zero-wind conditions, particularly with respect to expected temperature distributions. Because of the approximations inherent in a parabolic formulation of the pool fire problem, there are serious discrepancies between the model predictions and experimental data at low altitudes in the fire plume, but the level of accuracy of the model results increases markedly with vertical distance from the ground plane. While there is only a limited amount of experimental data available with which to compare model predictions, these data provide the most complete experimental data on large-scale pool fires that is currently available.

Specific results of the work described in this report are as follows:

1. An analytical model of large pool fires which is in good agreement with measured fire structure data has been developed. This model can be used as a tool for the analysis and interpretation of large-scale fire measurements and consumption of fibers in a large-scale fire.

2. Measured and computed temperature and species profiles show that significant unmixedness and incomplete combustion effects are present in large JP-4 pool fires.

3. Computational results indicate that the effects on fiber consumption of locally high temperatures because of temperature fluctuations in the fire are negligible; similarly the short residence time of fibers in regions of the fire calculation in which mean temperature is overpredicted compared to the measurements indicates that the overprediction of temperature in these regions should not greatly affect the overall fiber consumption prediction. There is, however, a need for further verification of the fiber consumption rate expression over a range of oxygen concentrations typical of a fire.

4. While particle thermal nonequilibrium can result in some temperature mismatch between the fibers and gas phase, the overall effects of nonequilibrium particle heat-up and cool-down tend to compensate resulting in only a small overall effect on particle consumption.

5. Based on the particle consumption expression defined in this report, overall single-fiber particle consumption of about 15% of the total particle mass is computed for large pool fires.

Further improvement of the mathematical modeling of the structure of a large pool fire over that described in this document requires recourse to a two- or three-dimensional elliptic Navier-Stokes formulation: beyond the complexity that such a formulation introduces of itself, establishment of appropriate boundary conditions for a more exact model is a difficult task. However. The use of an elliptic approach will allow the relaxation of the assumptions related to mixing rate that are incorporated in the present formulation, and such a model is the only valid method of treating in detail the phenomena in the lower part of the fire.

6. REFERENCES

1. "Assessment of Carbon Fiber Electrical Effects," NASA Conference Publication 2119, 1980.

2. Brzustowski, T. A. "The Hydrocarbon Turbulent Diffusion Flame in Subsonic Cross-Flow," AIAA Paper 77-222, AIAA 15th Aerospace Sciences Meeting, January 24-26, 1977.

3. "Analytical Prediction of Atmospheric Plumes and Associated Particle Dispersal Generated by Large Open Fires, Task II Interim Technical Progress Report," Report SAI-78-009-WH, prepared for NASA-Ames Research Center, Contract NAS2-10039, Science Applications, Inc., October 1978.

4. Harsha, P. T., Bragg, W. N. and R. B. Edelman. "Preliminary Report: Improvement of a Mathematical Model of a Large Open Fire," Report SAI-79-014-CP/R, prepared for NASA-Ames Research Center, Contract NAS-10327, Science Applications, Inc., September 1979.

5. Boccio, J. L., Weilerstein, G. and Edelman, R. B. "A Mathematical Model for Jet Engine Combustor Pollutant Emissions," NASA CR 121208, 1973.

6. Ferri, A., Libby, P. A., and Zakkay, V. "Theoretical and Experimental Investigation of Supersonic Combustion," Report ARL-62-467, September 1962, Aeronautical Research Laboratories, Wright-Patterson AFB, Ohio.

7. Harsha, P. T. "Free Turbulent Mixing: A Critical Evaluation of Theory and Experiment," AEDC TR-71-36, Arnold Engineering Development Center (AFSC) Arnold Air Force Station, Tenn., February 1971.

8. Alpinieri, L. J. "Turbulent Mixing of Coaxial Jets," AIAA Journal, Vol. 2, No. 9, September 1964, pp. 1560-1567.

9. Edelman, R. B., Fortune, O., and Weilerstein, G. "Analytical Study of Gravity Effects on Laminar Diffusion Flames," NASA-CR-120921, February 1972.

10. Lee, K. B., Thring, M. W., and Beer, J. M. "On the Rate of Combustion of Soot in a Laminar Soot Flame," Combustion and Flame, Vol. 6, pp. 137-145, 1962.

11. Gaydon, A. G. and Wolfhard, H. G. Flames, Their Structure, Radiation and Temperature, 2nd ed., London, Chapman & Hall Ltd., 1960.

12. Sparrow, E. M. and Cess, R. D., Radiation Heat Transfer, Belmont, Calif., Brooks/Cole Publishing Co., 1966.

13. Fortune, O. and Edelman, R. B. "The Effect of Mixing, Radiation, and Finite-Rate Combustion Upon the Flow Field and Surroundings of the Exhaust Plume of Rocket Engines Burning RP1 (Kerosene) and Liquid Oxygen." GASL-TR-681, General Applied Sciences Laboratories, 1967.